High resolution luminescence chronology of coastal dune deposits near Chumphon, Western Gulf of Thailand

Miocic, Johannes M.; Sah, Ritu; Chawchai, Sakonvan; Surakiatchai, Peerasit; Choowong, Montri; Preusser, Frank

Published in:
Aeolian Research

DOI:
10.1016/j.aeolia.2022.100797

Publication date:
2022

Aeolian Research 56 (2022) 100797

Contents lists available at ScienceDirect

Aeolian Research

journal homepage: www.elsevier.com/locate/aeolia

High resolution luminescence chronology of coastal dune deposits near Chumphon, Western Gulf of Thailand

Johannes M. Miocic [a,b,*], Ritu Sah [a], Sakonvan Chawchai [c,*], Peerasit Surakiatchai [c], Montri Choowong [c], Frank Preusser [a]

[a] Institute of Earth and Environmental Sciences, University of Freiburg, Freiburg, Germany
[b] Energy and Sustainability Research Institute Groningen, University of Groningen, Groningen, The Netherlands
[c] MESA Research Unit, Department of Geology, The Faculty of Science, Chulalongkorn University, Bangkok, Thailand

ARTICLE INFO

Keywords:
Coastal dune
Sedimentology
OSL dating
Sea-level change
Gulf of Thailand

ABSTRACT

The development of coastal dunes is linked to environmental controls such as sea-level variability, climatic conditions, and coastal morphology. Understanding the spatial and temporal variations of dunes is crucial for predicting how coastal landscapes may react to future climate changes and sea-level rise. However, there are very few detailed studies on the longer time-scale evolution (centennial to millennial) of coastal dunes from subtropical and tropical regions. Here, we combine a high-resolution luminescence chronology with sedimentological analyses to study the depositional history of a transverse coastal dune located within the Bang Berd dune field, Western Gulf of Thailand. While luminescence dating of uniform aeolian deposits is normally straight forward, we observe strong variations in the natural dose rate which are likely explained by the enrichment of accessory minerals in some laminae. Deposition of the dune started at least around 3000 years ago and coincides with a regional sea level drop. Sedimentary structures indicate deposition occurring predominantly in relation to the northeasterly winter monsoon. As the sea-level rise and increased storm intensity in the future may lead to stronger erosion along the coast, this study is highlighting the importance of the Bang Berd dune system as natural protection against coastal inundation.

1. Introduction

The ongoing global climate warming poses several threats to coastal areas, such as flooding and erosion, related to the predicted sea-level rise and the likely increase in storminess in some regions (Oppenheimer et al., 2019). Since many coastal zones are both economically important and densely populated, there is an inalienable need for establishing strategies of coastal management. Previous examples have shown that pure engineering-based measures are not always sustainable (e.g., Neal et al., 2018). This is explained by the fact that the complex interaction of local and regional sediment erosion, transport and deposition is often not fully understood and disturbed by engineering measures (e.g., Rangel-Buitrago et al., 2018). This can result in successional problems that might be even more severe than the original cause for action. Hence, understanding the sediment dynamics along coasts will help to design lasting solutions of coastal protection.

Dune fields are prominent features in sediment-rich coastal settings that form parallel to the beach line and represent a particular case of source bordering dunes. Their dynamics are controlled by the sea-level, sediment supply, and by erosion of the dune front during storm events (Pye, 1983). Accretion of the dune depends on supply of sand to a wide and dry beach across which sand can be mobilised by aeolian processes (Bauer and Davidson-Arnott, 2003; Sherman and Lyons, 1994). Coastal dune formation has been proposed to occur both in response to either sea level rise (e.g., Pye, 1983) or sea level fall (e.g., Lees, 2006). In the latter case, subaerial exposure of the former shoreface results in aeolian stripping of sediment from the beach to build foredunes. Other environmental factors such as storm frequency and strength (Bateman et al., 2018; Clemmensen et al., 2001; Sancho et al., 2012), beach profile and orientation (Miot da Silva and Hesp, 2010), vegetation (Hesp, 2004) and human impact may also exert control on dune formation.

Understanding the timing and rate of dune formation can help to decipher the controls on coastal sediment dynamics and several studies have used radiocarbon and optically stimulated luminescence (OSL)

* Corresponding authors at: Energy and Sustainability Research Institute Groningen, University of Groningen, Groningen, The Netherlands (J.M. Miocic); Department of Geology, The Faculty of Science, Chulalongkorn University, Bangkok, Thailand (S. Chawchai).
E-mail addresses: j.m.miocic@rug.nl (J.M. Miocic), Sakonvan.C@chula.ac.th (S. Chawchai).

https://doi.org/10.1016/j.aeolia.2022.100797
Received 17 November 2021; Received in revised form 14 February 2022; Accepted 10 March 2022
Available online 17 March 2022

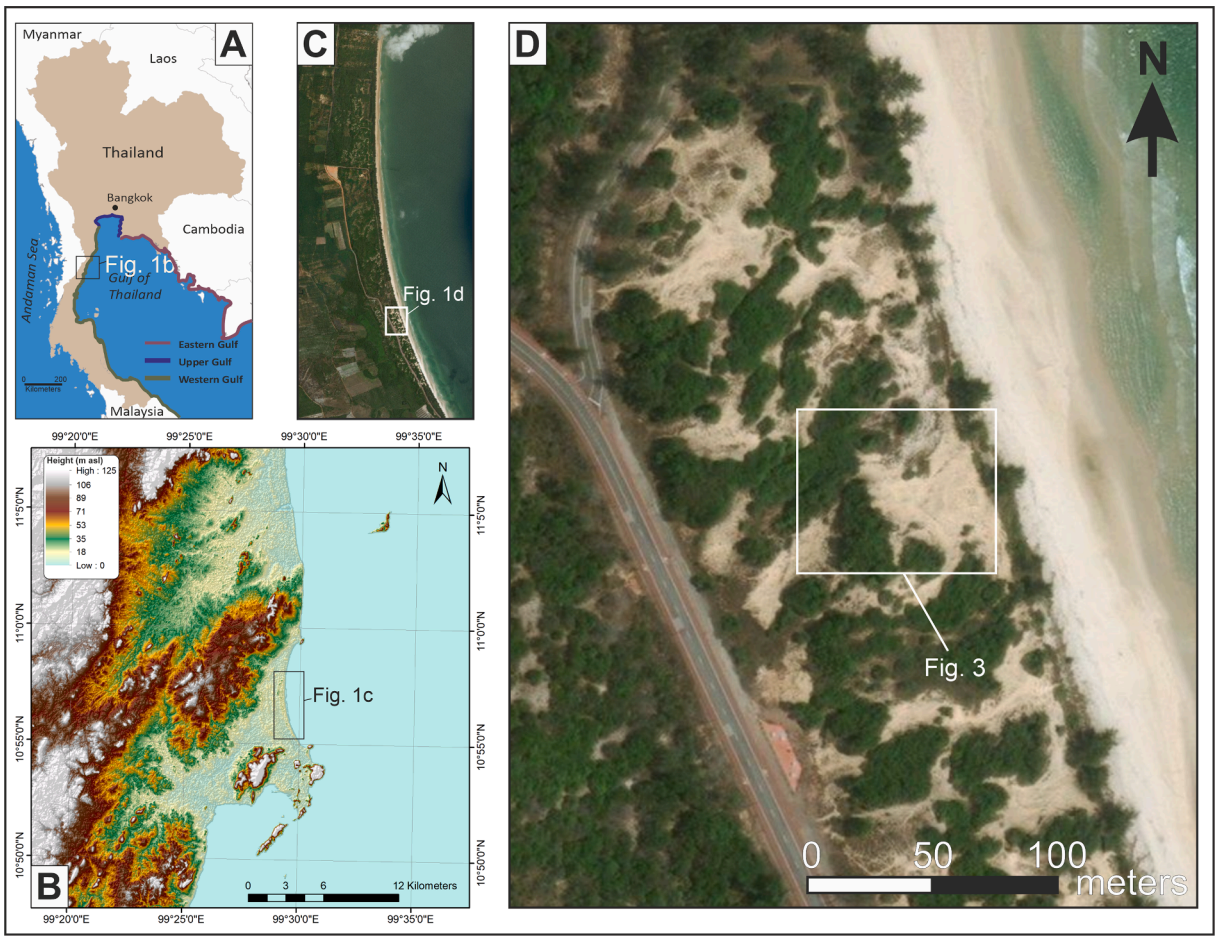

Fig. 1. Location of study site. A: Location within the Gulf of Thailand. B: DEM model of the northern Chumphon province with the Bang Berd Bay (NASA/METI/AIST/Japan Spacesystems and U.S./Japan ASTER Science Team, 2019). C, D: Satellite image of the investigated part of the Bang Berd dune field (© Bing Maps, Microsoft Cooperation).

dating to investigate coastal dune processes. The majority of coastal dune studies are located in temperate climates, for example, in Denmark (Clemmensen and Murray, 2006; Tindahl Madsen et al., 2007), the United Kingdom (Sommerville et al., 2007; Wilson et al., 2001), Canada (Neudorf et al., 2015), South Korea (Yu et al., 2009), and Japan (Tamura et al., 2011). Only a few studies have aimed at deciphering coastal dunes processes in tropical climates, with examples available from Vietnam (Tamura et al., 2020), India (Devi et al., 2013), and Thailand (Noppradit et al., 2019). These studies of tropical coastal dunes commonly have only a rather limited age data set for single dunes (e.g., Devi et al., 2013).

To further improve the understanding of how sedimentary dynamics within a tropical coastal system respond to sea level and climate changes, we identify the onset of dune formation and rates of sedimentation in a coastal dune of the Bang Berd dune field, Southern Thailand. Our study uses a combination of sedimentological investigation and high-resolution OSL chronology and represents the starting point for similar detailed investigations on the coastal sediment history along the shores of the Gulf of Thailand. Unexpected problems related to OSL dating require in-depth investigation and discussion of these phenomena. Besides the relevance regarding the interpretation of the present data set, these methodological observations have general implications related to OSL dating.

2. Study area

The Gulf of Thailand is a shallow semi-enclosed bay on the Sunda Shelf with a coastline of about 1900 km (Fig. 1). It can be divided into three parts: the Eastern, Upper, and Western Gulf. The coastal geomorphology of the Gulf of Thailand is variable but mainly characterised by coastal plains with sandy beaches and dunes, coastal wetlands (tidal flats, marshes and mangrove forest), or deltaic and estuary influence where large rivers flow into the ocean. Some areas represent rocky coasts with coastal cliffs. Climatically the region is dominated by the Asian monsoon system with a rainy season controlled by southwestern winds lasting from May to October. The winter season lasting from November to February is dominated by north-easterly winds, and the hot and dry season (transitional period from the NE to SW monsoons with average temperature of 30 °C) lasts from March to April. The SW monsoon brings warm and moist air from the Indian Ocean towards the SE Asia, resulting in an abundance of rainfall. Conversly, the NE monsoon transports cool and dry air from mainland China towards SE Asia, which causes rather temperate conditions in the North. However, in the southern part of Thailand, especially the lower part of Western Gulf (east coast), the NE monsoon normally causes mild weather and heavy rain, with its peak in November. For the Chumphon province, the mean annual rainfall ranges between 1700 and 2000 mm with a mean annual temperature of 26.7 °C (Saithong Silvicultural Research Station).

The ocean surface circulation within the Gulf of Thailand exhibits seasonal variations depending on the direction of the monsoon and an anti-cyclonic eddy near the western gulf centered at ca. 7°N exists throughout the year. During the NE monsoon, the sea level in the Gulf of Thailand is generally raised above mean sea level (MSL) because of seawater influx from the South China Sea resulting from the prevailing

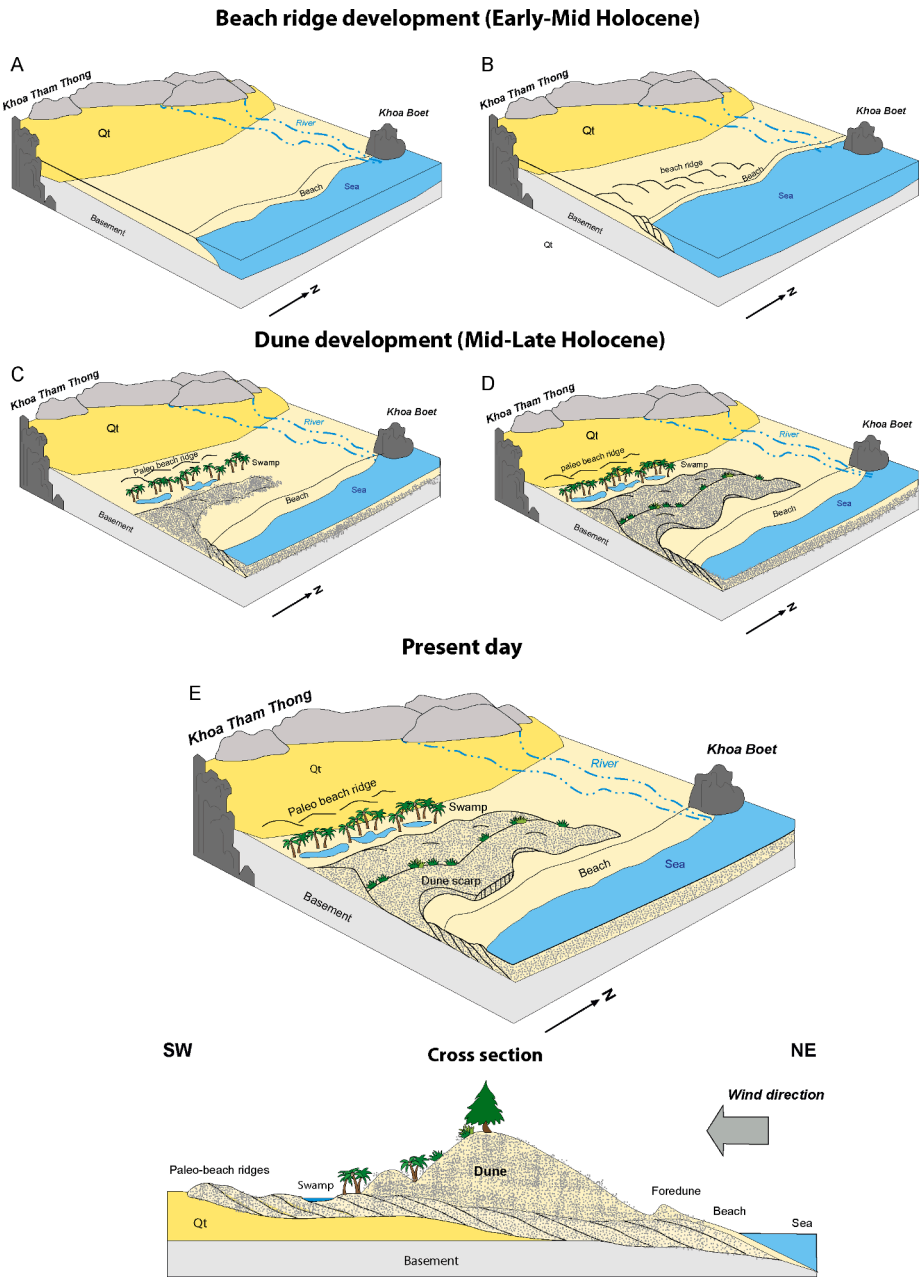

Fig. 2. Schematic model of the depositional environment evolution during the Holocene in the Bang Berd area drawn based on previous preliminary investigations by Prachantasen et al. (2008a,b), Lertnok et al. (2009) and Choowong (2011). A: Sea level rise during the Early Holocene leads to transgression onto the coastal plain. B: The Mid Holocene sea level high stand causes the development of a beach ridge along the shore line. C: Mid to Late Holocene sea level regression is accompanied by prograding beach ridges and the start of coastal dune formation. D: Late Holocene formation of the coastal dune field. E: Present day setting. Qt = terrace deposits (Quaternary).

northeasterly winds. In contrast, during the SW monsoon, wind blowing from the South leads to seawater efflux and thus a sea level within the Gulf of Thailand below MSL (Phantuwongraj et al., 2013). Additionally, during November–December, the eastern side of southern Thailand is regularly affected by depressions and tropical storms.

The study area is located in the Bang Berd Bay, Chumphon Province, in the Western Gulf of Thailand, about 430 km south of Bangkok (Fig. 1). The Bang Berd Bay coastline is formed by a ca. 10 km long, N-S oriented sandy beach of which northern and southern parts are truncated by headlands formed by outcropping limestones. Inland of the sandy beach a well-developed dune field has formed, with the highest dune ridges having an elevation of about 20 m above the present sea level. The dune field with an area of ca. 1 km^2 has a maximum width of 300 m and the highest dunes are generally located in its southern part. The dune field features three distinct dune sets: an inner set, which is located the most landwards and raises up to 6 m asl, a middle set, which contains the largest dunes, and a seaward set which contains smaller dune of up to 3 m height (Prachantasen et al., 2008a,b). In the southern part of the dune field only the inner and middle set occur while in the northern part a distinction into different sets becomes difficult as the topographic development is less clear. Based on aerial photography the dunes can be classified as predominantly parabolic and transverse, with the slip faces oriented landwards, indicating that the sand was deposited predominantly by easterly winds (Lertnok et al., 2009).

Plant communities covering the sands include coastal dune grassland (*Ipomoea imperati, Ipomoea pescaprae, Fimbristylis sericea, Cyperus stoloniferus)* and coastal scrub communities (e.g. *Sindora siamensis, Planchonella obovata, and S. grande* (Laongpol et al. 2009). Some climbers and herbs are also present (e.g. *Tetracera indica, Dunbaria bella and Dianella ensifolia*) (Laongpol et al., 2009). Shrubs and grasses mainly occupy the windward side, while the woody plant community (*Pandanus odorifer, Syzygium antisepticum and Syzygium grande*) favour the leeward side (Marod et al., 2020).

The dune field unconformably overlies beach ridges, which are also present several hundreds of meters inland where they form topographic heights. This unconformity can be clearly identified on ground-

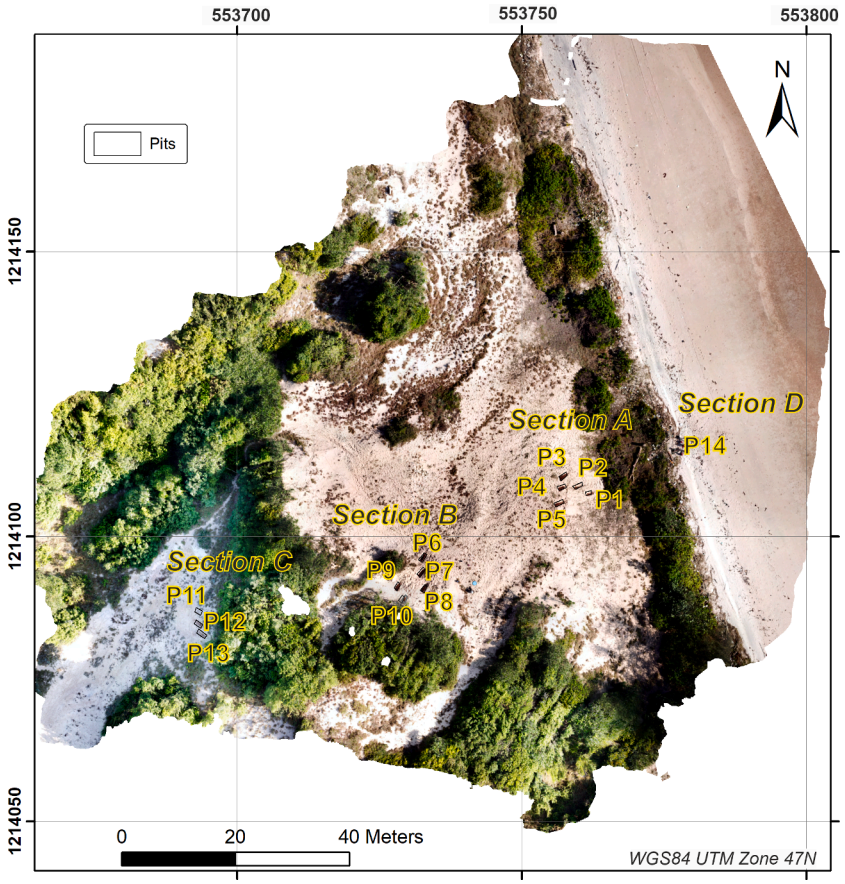

Fig. 3. Orthophoto of the studied dune showing the location of the pits (P1-P14) within the sections A-D.

penetrating radar profiles through the dune field (Lertnok et al., 2009). Other beach ridges 50 km south of the dune field indicate a regional sea level (RSL) fall from the Mid Holocene until around 3.8–1.6 ka based on OSL dating (Nimnate et al., 2015). Similarly, beach ridge ages around 150 km north of the study area indicate that RSL was apparently still dropping in the last 2 ka (Surakiatchai et al., 2018, 2019). Based on preliminary investigations of the sedimentary sequence and morphology at Bang Berg Bay (Choowong, 2011; Lertnok et al., 2009; Prachantasen et al., 2008a,b), as well as by considering the regional context, it is assumed that the dune development followed Early to Mid Holocene sea level changes which caused the formation of the beach-ridges (Fig. 2). Subaerial exposure and subsequent partial erosion of the beach ridges initiated the formation of a wide beach, from which aeolian erosion and transport inland led again to dune formation. However, the exact onset of dune formation and the rate of sedimentation is unknown.

3. Methods

3.1. Fieldwork

To investigate the depositional history, one of the largest individual dunes from the middle dune set in the southern part of the dune field was studied in detail. The dune flanks were sparsely vegetated which enabled the excavation of thirteen pits along the eastern (seaward) and northwestern dune face. The pits, with depths of 1.0–1.5 m, were partly overlapping with regards to elevation and enabled the creation of three continuous vertical profiles through the dune (Fig. 3): Section A (4.3–10.3 m asl) at the eastern base of the dune comprising pits 1 to 5, Section B (15.8–22.5 m asl) above Section A on the eastern flank of the dune including pits 6 to 10, and Section C (11.5–16.0 m asl) on the northwestern flank of the dune including pits 11 to 13. Due to a relatively flat topography between Sections A and B, which likely was due to a slope failure, it was not possible to have a continuous section through the east face of the dune. One additional pit was excavated on the backshore where a debris line indicated the storm tide line (Section D, pit 14). Locations of the pits were recorded by a levelling survey (Sokkia SET630R reflectorless total station) with regards to the mean sea level as well as by aerial photography using a drone (DJI Mavic Pro, Fig. 3). Photogrammetric analysis of the dune was hampered by the dense vegetation on all but the seawards part.

3.2. Sediment characterisation

After each pit was sedimentologically described and logged, a total of 30 samples for luminescence dating and grain size analysis were taken. Samples were collected by inserting a light-proof aluminium tube into the freshly exposed sediment. The contents of the tube were transferred into opaque sampling bags to avoid exposure and to retain moisture content. For dose rate determination additional samples of ca. 500 g were collected around the luminescence sample site. These samples were also used for grain size analyses.

For laser-optical grain size analysis no pre-treatment was necessary as the samples were very homogeneous and mainly composed of fine to medium sand. Grain size distribution was analysed with a Malvern Mastersizer 3000 and evaluated using GRADISTAT (Blott and Pye, 2001). Organic matter and carbonate content of the samples were analysed by loss on ignition (Heiri et al., 2001) using a muffle furnace with temperatures of 550 °C for 5 h for organic matter and 950 °C for 2 h for carbonate content.

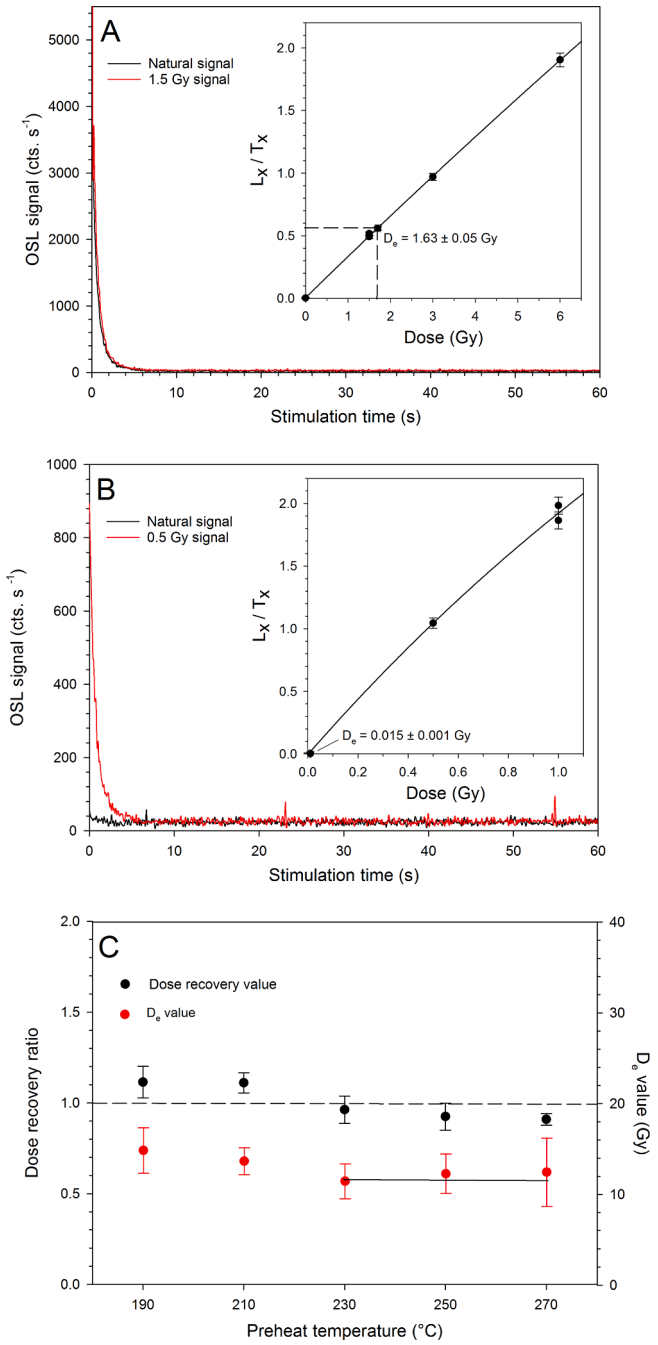

Fig. 4. Characterisation of OSL properties. A: Typical sample (CHU-4) showing a rather bright OSL signal and an almost identical shape of decay for the natural and laboratory irradiated OSL signal. Inset: The natural OSL signal is well placed on the dose response curve. B: A very young sample (CHU-30) with very low OSL signal level observed for the natural signal in comparison to the OSL signal resulting from laboratory irradiation. The natural OSL signal is very close to zero and the D_e estimate should be only regarded as semi-quantitative. C: The results of OSL performance test reveal the best dose recovery for a preheat at 230 °C. The preheat test shows a plateau starting at 230 °C.

3.3. Luminescence dating

Initial preparation work was done at the red-light laboratory at Chulalongkorn University, Bangkok. The water content was first measured and samples were subsequently dry sieved (105–177 μm), followed by removal of carbonate and organic material using hydrochloric acid and hydrogen peroxide, respectively. Heavy minerals were removed using a magnetic separator. The samples were then transferred to Freiburg, and then etched by 40% hydrofluoric acid for one hour to remove the outer layer of the mineral surface that is affected by alpha radiation and to purify the quartz grains. Dried grains were mounted on stainless steel discs using a 2 mm stamp of silicon oil (ca. 50 grains per aliquot).

Luminescence measurements were performed on an automated TL/OSL-DA-15 Risø reader fitted with a bialkali EMI photomultiplier and a $^{90}Sr/^{90}Y$ beta source (ca. 0.1 Gy s^{-1}). Equivalent dose (D_e) measurements were carried out using the single-aliquot regenerative-dose protocol (SAR) of Murray and Wintle (2000), applying preheating at 230 °C for 10 s as identified appropriate in different tests (Fig. 4C). Most of the samples show bright OSL signals and an excellent performance during the SAR protocol (Fig. 4A) and 24 replicate measurements were used for statistical analyses. However, for some very young samples, the SAR

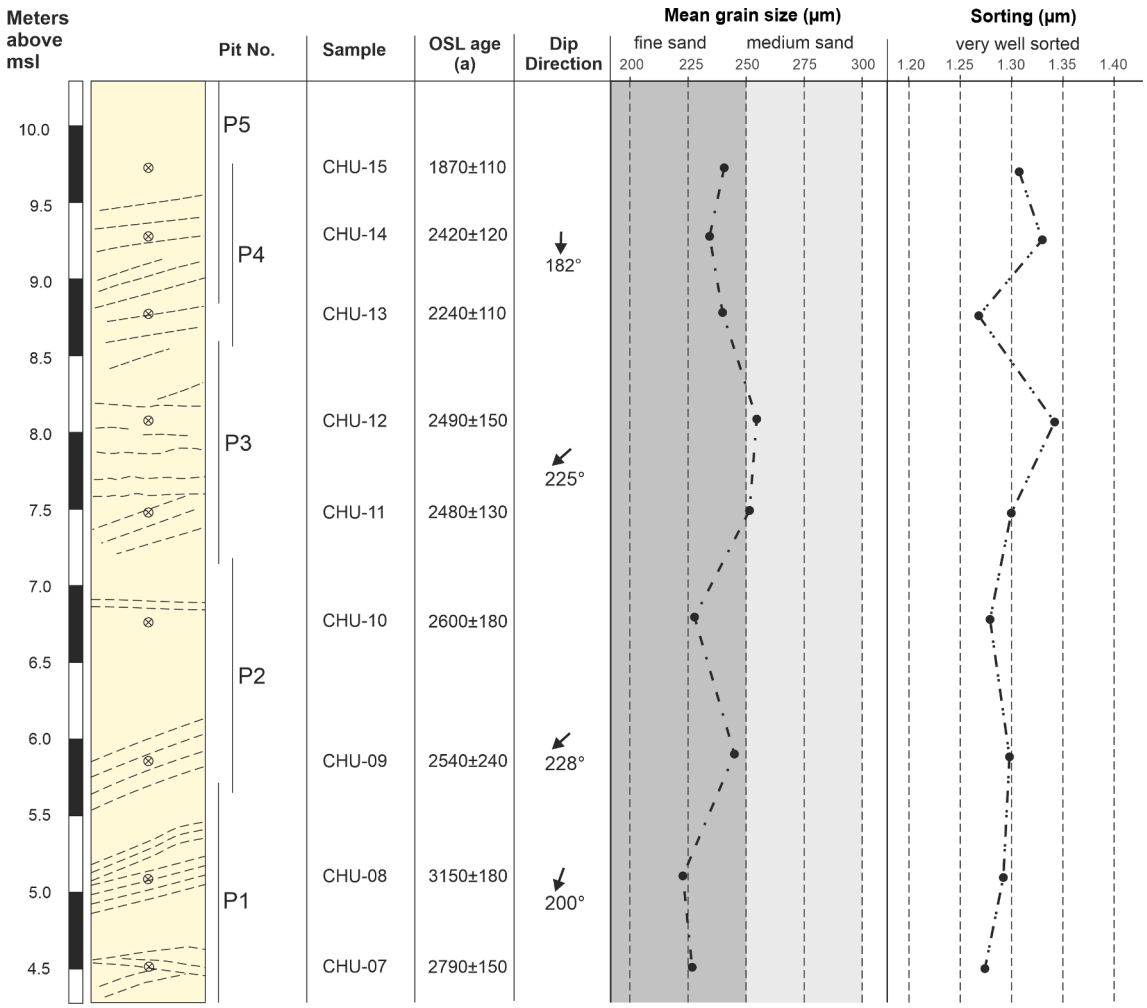

Fig. 5. Combined sedimentological log of section A.

protocol had to use low irradiation doses (0.5 and 1 Gy), which led to problems for some aliquots with regard to OSL signal counting statistic. For young samples quantification of the OSL signal close to background (i.e., calculating a D_e) is also not straightforward (Fig. 4B). In this case, the number of replicate measurements was increased to 48. For several samples, some aliquots had to be rejected due to poor quartz luminescence sensitivity or not passing the SAR quality criteria (recycling ratio within 10% of unity, test dose error < 10%, IR depletion ratio < 10%). D_e calculation was conducted based on using either the Central Age Model (CAM) or the Minimum Age Model (logged MAM-3; Galbraith et al., 1999), using the r-script by Burow (2020a, 2020b). The determination of the appropriate age model was based on the shape of the D_e distribution and the observed overdispersion (see below).

The determination of the concentration dose-rate relevant elements (K, Th, U) was carried out at VKTA (Radiation Protection, Analytics & Disposal Rossendorf Inc.) in Dresden, using high-resolution gamma spectrometry (cf. Preusser and Kasper, 2001). No evidence for radioactive disequilibrium in the uranium decay chain was observed. Dose rates and ages were calculated using the software ADELE v2017 (Degering and Degering, 2020; https://www.add-ideas.de), which uses the dose rate conversion factors of Guerin et al. (2011). An average water connent during burial time of 2–8% has been assumed (measured water conents were 2–4%). Cosmic-ray dose rates were corrected for geographic position and burial depth following Sherman and Lyons (1994).

4. Results and interpretation

4.1. Sedimentology

The parabolic to hummocky dune consists of well to very well sorted, fine to medium sands with mean grain size varying from 199 µm to 255 µm (Figs. 5–7). The sands contain very little organic matter (0.02–0.26 %) and also have very low carbonate contents (0.02–0.10 %). The organic matter likely originates from rootlets which are commonly visible in the pits. The sand in the top ca. 20 cm of each pit is often unstructured, dominated by rootlets, and of lighter colour than the deeper parts of the pits. These sections are interpreted to result from local erosion and reworking of the dune and are not taken further into account. Sedimentary structures within the light-yellowish-brownish sands are made visible by the enrichment of dark minerals in some laminae (Fig. 8). Cross bedding, with angles of 19-40°, is common, as are faint ripple structures which are observed in the cross section. If dark minerals are missing, the sands appear structureless and massive. Individual cross bed sets have thicknesses of up to 0.5 m and are regularly truncated by another set of cross beds.

Section A (Fig. 5) is dominated by cross beds (4.3–7.5 m, 8.2–10.3 m) with the central section containing ripple structures (7.5–8.2 m). Dip direction of the cross beds is predominantly south to southwest. At the base of Section B (Fig. 6) one set of cross beds dips towards north while the overlying cross beds all dip towards south and southwest. The lower part of Section B (15.8–17.1 m) has a distinctly darker colour (dark brown to grey) than the upper part where the sands have the same light

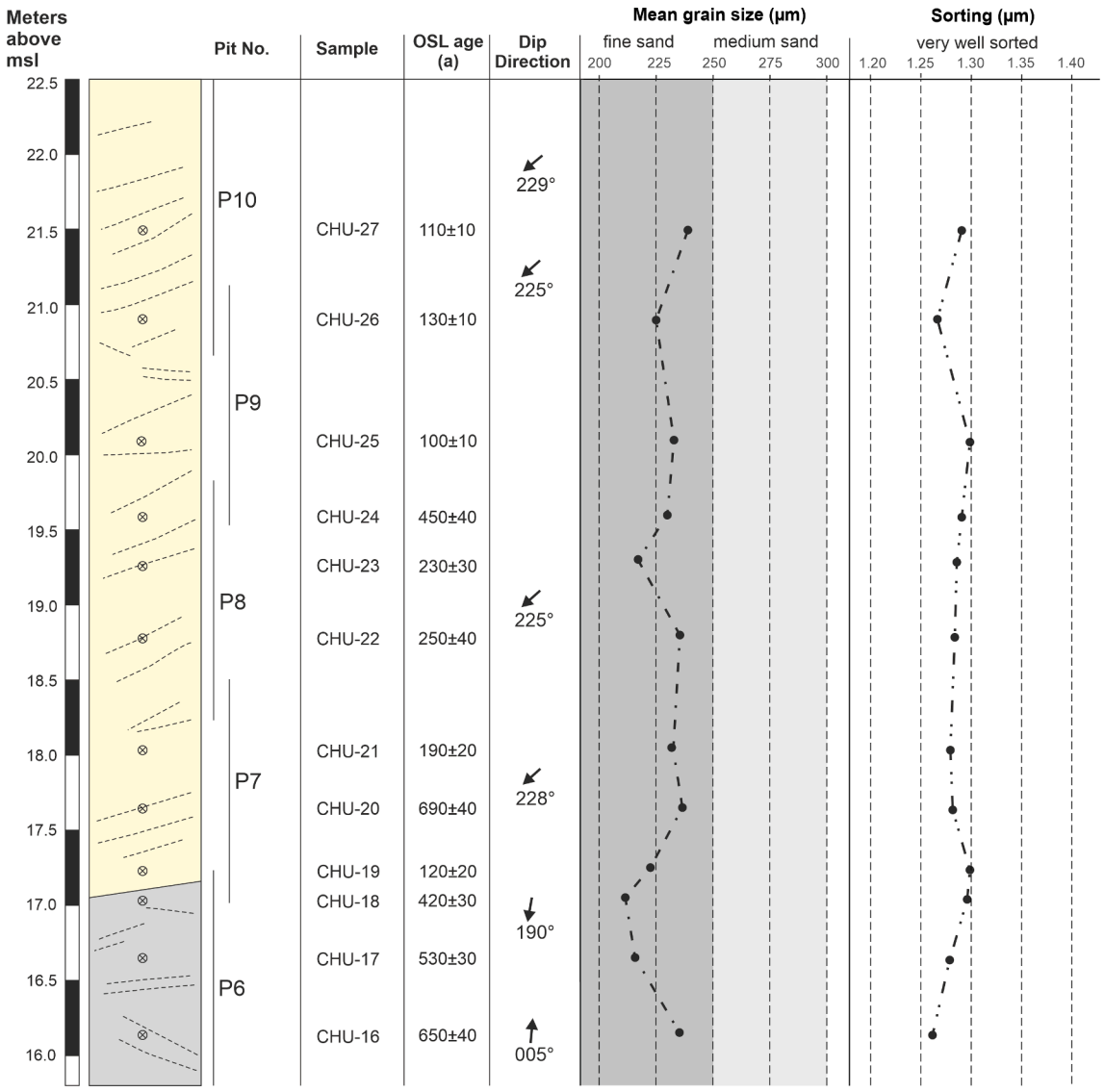

Fig. 6. Combined sedimentological log of section B.

yellowish-brownish colour as in the other sections. The colour transition is very sharp and the contact is dipping towards south-west. The darker colour originates from a higher content of iron-(hydr)oxides (limonite, goethite, hematite) which have been identified under the microscope. Sands in Section C (Fig. 7) have the same light yellowish-brownish colour as the other sections but have fewer laminae, enriched in dark minerals, and subsequently the identification of sedimentary structures as well as their dipping direction was hindered.

Section D (Fig. 8) shows parallel bedded layers of yellowish-brownish sand with some layers consisting predominantly of black minerals. Plastic debris, wood fragments, and parts of fishing nets are common in the darker layers. The beds are slightly (<3°) dipping towards the sea at approximately the same angle as the beach and some of the layers show some post-depositional deformation.

The crossbeds observed in all three sections dissecting the internal structure of the dune are interpreted as foresets dipping downwind, with the foresets with high apparent dips likely to be produced by grain-flow deposition on the slip face (Pye and Tsoar, 2009). The individual crossbeds of thicknesses < 1 m are thought to represent smaller scale dunes superimposed on larger parabolic to transverse dunes while the thick (>2–3 m) beds indicate migration of the dune slip surface. The observed ripples are interpreted as climbing ripples formed on the upwind side of the dune. The enrichment of accessory minerals in the grain flow foreset laminae is either due to the separation of denser minerals during the grain flow or related to changes in wind-speed which results in the preferential transportation of the denser minerals. Enriched heavy-mineral concentrations are commonly observed in aeolian deposits and have been linked to local increase in near-surface turbulence at the crest of ripples (Buynevich, 2012) and the cyclic variation of the angle of climb in a climbing-wind-ripple (Hunter and Richmond, 1988). Note that the type of dominant mineral in the laminae is not coinciding with a change in grain-size. This is likely because only a very narrow bandwidth of grain size is being sourced from the beach. In fact, the samples from pit 14, on the backshore, demonstrate overall very similar grain-size parameters as the aeolian sands from the dune. This is in line with previous research which highlights that the beach setting controls aeolian delivery to coastal dunes (Bauer and Davidson-Arnott, 2003; Miot da Silva and Hesp, 2010; Sherman and Lyons, 1994). The lower part of Section B with the darker colour presence of iron-(hydr) oxides is interpreted as a palaeosoil horizon, which is eroded by a first order bounding surface which marks the start of a new phase of sediment aggregation. Deposition mainly occurred in relation to north-easterly wind conditions, with the vast majority of foresets dipping towards the SW. One exception can be found at the base of Section B,

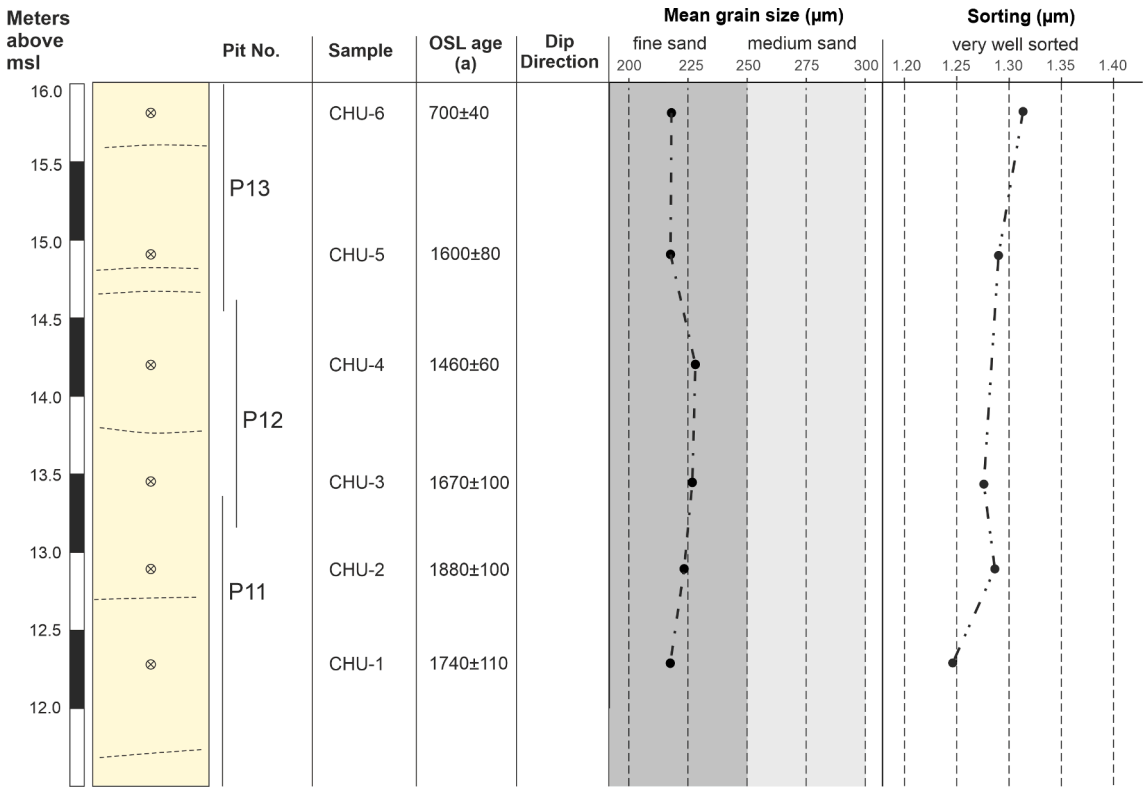

Fig. 7. Combined sedimentological log of section C.

where a foreset dips towards NE and was thus likely deposited during prevailing SW wind.

The sedimentary features observed in the backshore pit (section D) are thought to illustrate individual storm events, with each of the laminae set enriched in anthropogenic debris and heavy minerals caused by higher transport energy. This is in line with sedimentary features known to be linked to coastal storms such as (1) many individual laminae per storm event, (2) planar laminations, (3) abrupt basal contacts, and (4) debris (Morton et al., 2007). The laminae set between the storm events represent the normal backshore sedimentation, likely caused mainly by aeolian processes which also source the dune further landwards.

4.2. OSL dating

A consistent set of ages was expected considering the excellent properties of the OSL signal and, at first glance, the homogenous nature of the sediment. On the contrary, the data set features scattering and a number of inversions that will be discussed further below (Table 1; Fig. 9A). With regard to the basic data that is used to calculate ages, two observations are striking. First, dose-rate relevant elements in the different samples show a large variance that results in a spread of annual dose rates from 0.59 ± 0.04 Gy ka^{-1} (CHU-1) to 3.88 ± 0.21 ka^{-1} (CHU-8). While the latter is a solitary extreme value, several samples are three to four times larger than the lowest value (Fig. 9B). For further analyses, it is important to consider which kind of radiation is contributing to the total dose rate. In the present context these are β- and γ-rays as well as cosmic radiation (comprising a wide range of primary and secondary rays), as the contribution of α-radiation has been removed by HF-etching of the quartz grains. The cosmic dose rate depends on the burial depth which was between 10 cm and 150 cm in the present case. This results in a cosmic dose rate between 0.15 Gy ka^{-1} (CHU-6) and 0.20 Gy ka^{-1} (CHU-26). The remaining dose rate results from β- and γ-radiation and the contribution to the total dose rate by the former is rather constant with about 37 ± 2% on average (Fig. 9C). In contrast, the origin of β-radiation shows quite some variation (Fig. 9D–F) and a synchronous trend for increasing contribution from Th and U with an opposing trend for K. Overall, the variation in the K-concentration (between 0.10 ± 0.01% and 0.24 ± 0.02%; mean = 0.14 ± 0.04%, RSD = 30%) is much lower than for Th (2.49 ± 0.18 ppm to 31.20 ± 1.90 ppm; mean = 6.20 ± 5.88 ppm, RSD = 95%) and U (0.59 ± 0.04 ppm to 3.88 ± 0.21 ppm; mean 1.29 ± 1.13 ppm, RSD = 87%).

Plotting the concentration of Th- versus U-concentration in the samples investigated reveals a linear relationship, at a ratio of ca. 5:1 (Fig. 10). Since Adams and Weaver (1958), U/Th ratios have been used as indicators of provenance and the constant ratios observed here imply a common source of both elements. As the sediment is mainly composed of quartz, bears almost no carbonates, organic material or minerals sensitive to weathering such as feldspar (shown by the low K-concentration), Uranium and Thorium will presumably be present in stable heavy minerals. The presence of such minerals is likely reflected by the dark layers observed in the sediment exposure (Figs. 5–8). Optical inspection did not allow proper identification of the type of mineral. However, zircon as an extremely weathering resistant mineral in which, Thorium and Uranium occur in abundances ranging from tens to thousands of parts per million (Speer, 1980), is the probable candidate. Hence, the large differences in dose rate are likely explained by a varying content of zircon in the sediment. This could be either related to primary flux of zircon into the sediment system, or by a mechanical separation effect such as wind strength; the density of zircon (4.6–4.7 g cm^{-3}) is almost double that of quartz.

The second interesting observation regarding the OSL data set is related to the fact that the samples show a quite different degree of scatter in the individual D_e data sets (Fig. 11). This is reflected by the overdispersion value, i.e., the presence of greater variability than expected from counting statistic instrumental reproducibility, which can be quantified (cf. Galbraith and Roberts, 2012). The values observed for the samples under consideration range from 0.07 to 0.54. The overdispersion of D_e value data sets observed in sediment samples is ususally explained by the effect of sediment mixing (e.g., Tribolo et al., 2010),

Fig. 8. Image of pit 14 (Section D) on the backshore, facing landwards towards the studied dune. Layers with a high content of dark minerals are clearly visible (white arrows), as is plastic debris and parts of fishing nets (yellow arrows). Sample locations of OSL samples CHU28 to CHU30 are indicated, as are their OSL ages. (For interpretation of the references to colour in this figure legend, the reader is referred to the web version of this article.)

microdosimentry (e.g., Mayya et al., 2006), and/or partial resetting of the OSL signal prior to deposition (e.g., Olley et al., 2004). Due to the nature of sediments and the observed intact sediment structures, the first appears as an rather unlikely explanation. Furthermore, the non-Gaussian shapes of the different D_e distributions are all positively skewed (Fig. 11). Interestingly, the D_e distributions of the three samples taken from beach sand sandwitched between modern storm deposits (CHU-28 to CHU-30; containing plastic debris) show little evidence for significant partial bleaching, i.e. values much higher than the rest. The highest individual D_e values determined for aliquots from these deposits are 0.25 ± 0.02 Gy for CHU-28 and 0.16 ± 0.02 for CHU-29. All other aliquots (n = 97) are not exceeding D_e values of 0.1 Gy. On the other hand, there appears to be also no direct relationship between dose rate and overdispersion (Fig. 12A), which could explain the observed scatter in D_e values. It is also shown that while for part of the samples the highest D_e value is part of the main (median) distribution (Fig. 12B), several samples show outliers that are more than one order of magnitude higher than the median value. The most likely explanation appears, as dose rate is not a suitable candidate, to attribute these outliers to partical bleaching. This is despite the fact that the three modern samples do not show such a degree of scattering.

Nevertheless, while the number of D_e-values outside a Gaussian-like distribution at the upper edge is rather low (Fig. 11A, B, D, E), it appears necessary to remove these values when calculating mean D_e. All samples without positively skewed distributions (example in Fig. 11C) have overdispersions between 0.09 and 0.12 (Table 1), wich the exception of sample CHU-30 (overdisperion = 0.07; Fig. 11F). However, the latter sample is characterised by large individual D_e uncertainties that will lead to a lower overdispersion. Hence, a value of 0.12 was used for the sigma_b value in the MAM calculations and these were only carried out for samples in which the overdisperion is higher than this value.

4.3. Chronology of aeolian deposition

The high vertical resolution of age data allows for a detailed analysis of the depositonal chronology. We applied a widely-used age-depth modelling approach, which is based on Bayesian statistics (Blaauw and Christen, 2011), to reconstruct the accumulation history for the studied dune (Fig. 13). First, the model was computed based on the OSL data alone as reference (Fig. 13A). The second age-depth model (Fig. 13B) does also take sedimentological observations as well as breaks in the age data set into account, interpreting both as breaks in deposition. Deposition of the dune recorded in the studied sections started at least ca. 3000 years ago and continued with a steady accumulation rate of 0.6 cm per year until around 1200 years ago.

Following the first long period of accumulation, a sedimentation hiatus, potentially with a period of erosion, occurred between samples CHU-5 (1600 ± 80 a) and CHU-6 (700 ± 40 a) at ca. 650 cm depth (ca. 15.5 m asl). Note that the sands within the pit which covers this depth are massive and structureless and thus provide no evidence for or against this hiatus, noted as Hiatus A in the discussion, from the sedimentological point. However, without an erosional feature or hiatus, the sedimentation rate between samples CHU-5 and CHU-6 would be only 0.1 cm per year. As there are no indications of soil development between the two samples, which would be expected at such low sedimentation rates, a hiatus is assumed. Sedimentation restarted at ca. 700 years ago and continued until ca. 420 years (480 cm depth, 17.2 m asl) with a similar sedimentation rate of 0.6 cm per year, where the development of a palaeosoil indicates a depositional hiatus of at least several decades. This hiatus is denoted as Hiatus B in the discussion. The ages determined

Table 1
Summary data of OSL dating indicating the sampled section, elevation above mean sea-level, sediment cover as used for the calculation of cosmic dose rate, the concentration of dose rate relevant elements (K, Th, U), the total dose rate, the number of aliquots (n: measured/passing the rejection criteria), the observed over-dispersion, mean D_e calculated by the Central Age Model (CAM) and the Minimum Age Model (MAM). The latter was used for age calcuation only if the observed overdispersion exceeds 0.12.

Sample	Section	Elevation (cm)	Cover (cm)	K (%)	Th (ppm)	U (ppm)	D (Gy ka^{-1})	Aliquots n	Over-dispersion	CAM D_e (Gy)	MAM D_e (Gy)	Age (a)
CHU-1	A-1	1230	120	0.13 ± 0.01	2.49 ± 0.18	0.54 ± 0.14	0.59 ± 0.04	24/23	0.17	1.04 ± 0.04	1.02 ± 0.04	1740 ± 110
CHU-2	A-1	1290	60	0.16 ± 0.01	5.10 ± 0.33	0.95 ± 0.18	0.91 ± 0.05	24/24	0.14	1.74 ± 0.05	1.71 ± 0.05	1880 ± 100
CHU-3	A-2	1345	120	0.15 ± 0.01	3.80 ± 0.26	1.04 ± 0.21	0.81 ± 0.06	24/24	0.27	1.45 ± 0.08	1.36 ± 0.04	1670 ± 100
CHU-4	A-2	1420	50	0.15 ± 0.01	6.46 ± 0.40	1.30 ± 0.16	1.08 ± 0.05	24/24	0.09	1.58 ± 0.03	–	1460 ± 60
CHU-5	A-3	1490	100	0.12 ± 0.01	9.90 ± 0.60	1.90 ± 0.30	1.42 ± 0.07	24/24	0.10	2.28 ± 0.05	–	1600 ± 80
CHU-6	A-3	1580	30	0.10 ± 0.01	8.10 ± 0.50	1.55 ± 0.24	1.26 ± 0.06	24/24	0.11	0.88 ± 0.02	–	700 ± 40
CHU-7	B-1	450	120	0.12 ± 0.01	3.61 ± 0.24	0.93 ± 0.17	0.75 ± 0.04	24/24	0.09	2.08 ± 0.04	–	2790 ± 150
CHU-8	B-1	510	60	0.13 ± 0.01	31.20 ± 1.90	5.90 ± 0.60	3.88 ± 0.21	24/19	0.15	12.51 ± 0.45	12.23 ± 0.45	3150 ± 180
CHU-9	B-2	590	120	0.17 ± 0.02	2.70 ± 0.19	0.56 ± 0.12	0.64 ± 0.06	24/21	0.12	1.63 ± 0.05	–	2540 ± 240
CHU-10	B-2	680	30	0.13 ± 0.01	2.91 ± 0.20	0.64 ± 0.17	0.67 ± 0.04	24/23	0.18	1.79 ± 0.07	1.75 ± 0.07	2600 ± 180
CHU-11	B-3	750	100	0.23 ± 0.02	2.75 ± 0.19	0.56 ± 0.12	0.71 ± 0.04	24/20	0.18	1.83 ± 0.07	1.75 ± 0.05	2480 ± 130
CHU-12	B-3	810	40	0.24 ± 0.02	3.58 ± 0.23	0.70 ± 0.15	0.83 ± 0.05	24/20	0.17	2.06 ± 0.08	1.95 ± 0.11	2490 ± 150
CHU-13	B-4	880	70	0.16 ± 0.01	2.50 ± 0.17	0.56 ± 0.11	0.63 ± 0.04	24/23	0.18	1.45 ± 0.06	1.41 ± 0.03	2240 ± 110
CHU-14	B-5	930	120	0.21 ± 0.02	4.20 ± 0.28	0.86 ± 0.12	0.85 ± 0.04	24/23	0.13	2.12 ± 0.06	2.07 ± 0.06	2420 ± 120
CHU-15	B-5	975	75	0.21 ± 0.02	3.74 ± 0.24	0.73 ± 0.14	0.80 ± 0.05	24/24	0.19	1.55 ± 0.06	1.50 ± 0.04	1870 ± 110
CHU-16	C-1	1615	100	0.14 ± 0.01	2.61 ± 0.18	0.76 ± 0.12	0.66 ± 0.04	24/22	0.18	0.47 ± 0.02	0.43 ± 0.02	650 ± 40
CHU-17	C-1	1665	50	0.13 ± 0.01	7.70 ± 0.50	1.70 ± 0.21	1.24 ± 0.08	24/23	0.15	0.68 ± 0.02	0.66 ± 0.03	530 ± 30
CHU-18	C-1	1705	10	0.14 ± 0.01	9.90 ± 0.60	2.04 ± 0.26	1.54 ± 0.09	24/24	0.18	0.67 ± 0.03	0.65 ± 0.03	420 ± 30
CHU-19	C-2	1725	90	0.18 ± 0.01	5.05 ± 0.40	1.11 ± 0.19	0.98 ± 0.09	24/23	0.20	0.13 ± 0.01	0.12 ± 0.01	120 ± 20
CHU-20	C-2	1765	40	0.13 ± 0.01	2.81 ± 0.20	0.70 ± 0.13	0.67 ± 0.04	24/24	0.35	0.51 ± 0.04	0.46 ± 0.02	690 ± 40
CHU-21	C-2	1805	30	0.13 ± 0.01	4.04 ± 0.27	0.92 ± 0.17	0.81 ± 0.07	24/20	0.28	0.18 ± 0.01	0.16 ± 0.01	190 ± 20
CHU-22	C-3	1880	130	0.16 ± 0.01	2.66 ± 0.19	0.45 ± 0.10	0.60 ± 0.08	48/23	0.49	0.17 ± 0.01	0.15 ± 0.01	250 ± 40
CHU-23	C-3	1930	80	0.14 ± 0.01	4.50 ± 0.30	1.04 ± 0.17	0.86 ± 0.09	48/24	0.54	0.24 ± 0.02	0.20 ± 0.02	230 ± 30
CHU-24	C-4	1960	140	0.14 ± 0.01	3.27 ± 0.23	0.64 ± 0.14	0.67 ± 0.05	48/40	0.40	0.36 ± 0.03	0.30 ± 0.02	450 ± 40
CHU-25	C-4	2010	90	0.17 ± 0.01	5.50 ± 0.40	1.31 ± 0.20	1.02 ± 0.11	48/42	0.18	0.11 ± 0.01	0.10 ± 0.01	100 ± 10
CHU-26	C-5	2090	150	0.12 ± 0.01	3.19 ± 0.22	0.67 ± 0.13	0.65 ± 0.06	48/16	0.30	0.087 ± 0.007	0.083 ± 0.007	130 ± 10
CHU-27	C-5	2150	90	0.16 ± 0.01	3.31 ± 0.22	0.68 ± 0.12	0.71 ± 0.04	48/36	0.12	0.074 ± 0.002	–	110 ± 10
CHU-28	D-1	120	70	0.07 ± 0.01	16.00 ± 0.90	3.50 ± 0.40	2.14 ± 0.24	48/29	0.48	0.043 ± 0.005	0.038 ± 0.004	18 ± 2
CHU-29	D-1	155	35	0.08 ± 0.01	7.20 ± 0.50	1.55 ± 0.24	1.11 ± 0.10	48/35	0.35	0.017 ± 0.004	0.012 ± 0.001	11 ± 1
CHU-30	D-1	180	10	0.04 ± 0.00	15.30 ± 1.00	3.00 ± 0.40	1.90 ± 0.15	48/34	0.07	0.015 ± 0.001	–	8 ± 1

for the top most section of the dune (<480 cm depth, >17.2 m asl) are characterised by some inversions, in particular samples CHA-20 (690 ± 40 a) and CHA-24 (450 ± 40 a), which are significantly older than the other ages determined for this part of the sequence (strechting from 250 to 100 a). However, the pattern of D_e distribtions for these two samples are quite similar to the other samples as are the overdispserion values and annual dose rates (Table 1). Since these samples are way out of the range of the other ages determined for this part, these have been treated as outliers and are not considered in the second age model (Fig. 13B). While, sample CHU-19 is also slightly off (120 ± 20 a) compared to the other ages in this part (ca. 200–250 a) including or removing this has little impact on the age model. Lastly, accumulation of this part of the sequence took place between ca. 250 and 100 years ago, with an accumulation rate of ca. 3 cm per year.

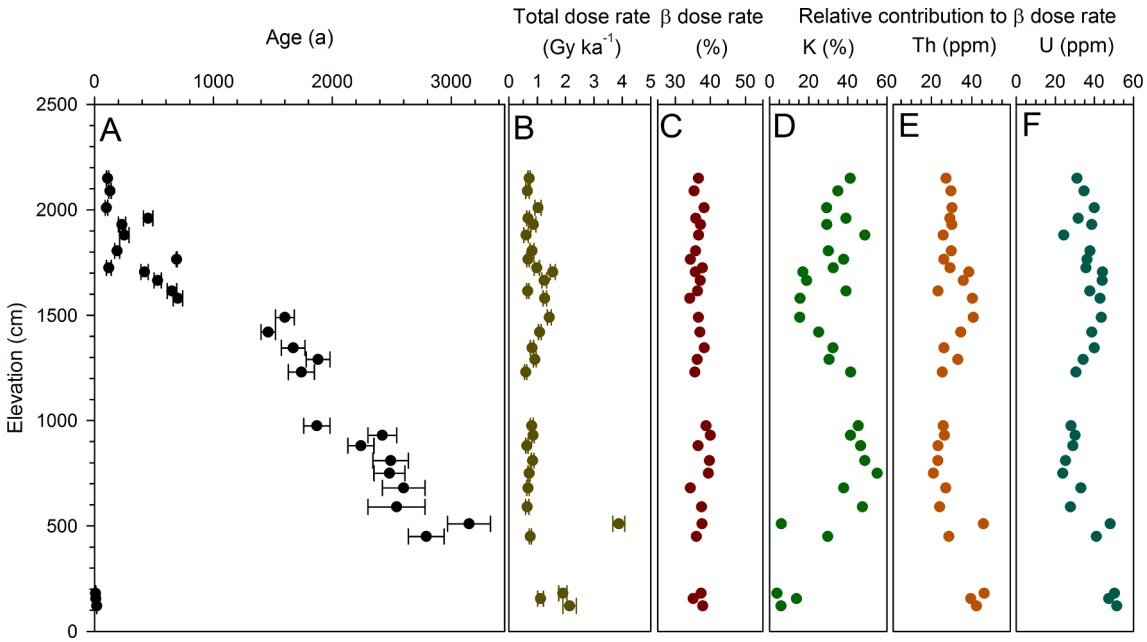

Fig. 9. A: OSL ages versus elevation above mean sea-level. Please note that the three samples between 100 and 200 cm are from young storm deposits (including plastic waste) at the foot of the dune sequence. B: The total dose rate of the samples shows a large degree of variation, in particular generally higher values for the storm deposits. One extreme value of 3.88 ± 0.21 Gy ka^{-1} for sample CHU-8 is five time higher as the typical values determined for the dune samples (mainly between 0.5 and 1.0 Gy ka^{-1}). C: The contribution of beta radiation to the total dose rate is relatively constant (37 ± 2%). D-F: The origin of beta particles from the different elements (K, Th, U) shows a large variation.

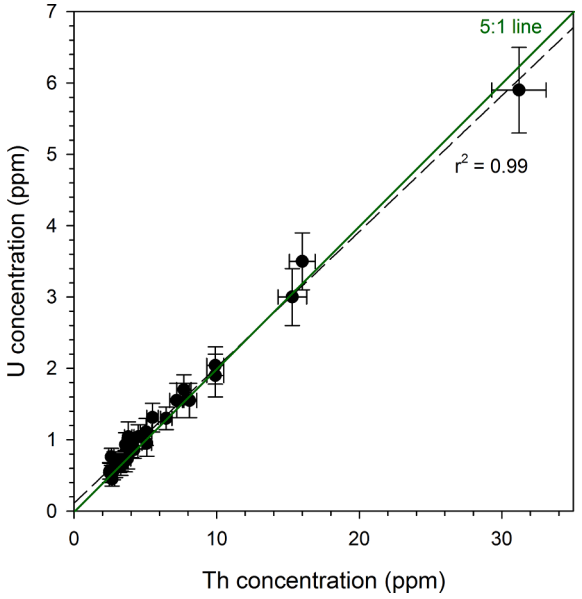

Fig. 10. Comparison of Th and U concentration in the samples reveals a linear relationship at the ratio 5:1.

5. Discussion

5.1. Dune formation and sea-level change

The onset of the formation of the investigated costal dune around at least 3000 years ago (mid-late Holocene) poses the question of a possible link to relative sea level (RSL) changes in the study region. Indeed, records of past RSL changes in SE Asia are common and combining many studies resulted in extensive and detailed RSL datasets (e.g. Bird et al., 2010, 2007; Brill et al., 2015; Choowong et al., 2004; Hesp et al., 1998; Horton et al., 2005; Meltzner et al., 2017; Parham et al., 2014; Scheffers et al., 2012). These and other studies have recently been compiled into a standardised Holocene RSL database for broader SE Asia, including the Maldives, India and Sri Lanka (SEAMIS) (Mann et al., 2019). The resulting sea level curves indicate a RSL rise from below −30 m at the start of the Holocene to the maximum mean sea level at ca. 7 ka, with a 2–5 m higher than present RSL being recorded between 6 ka and 4 ka. After 4 ka sea level has been falling until present RSL was reached ca. 2 ka ago (Fig. 14). The onset of coastal dune formation in the Western Gulf of Thailand at least around 3000 years ago indicates that RSL at that time was at least close to present day msl (or lower) as a wide, dry beach is needed to provide source material for the dune formation.

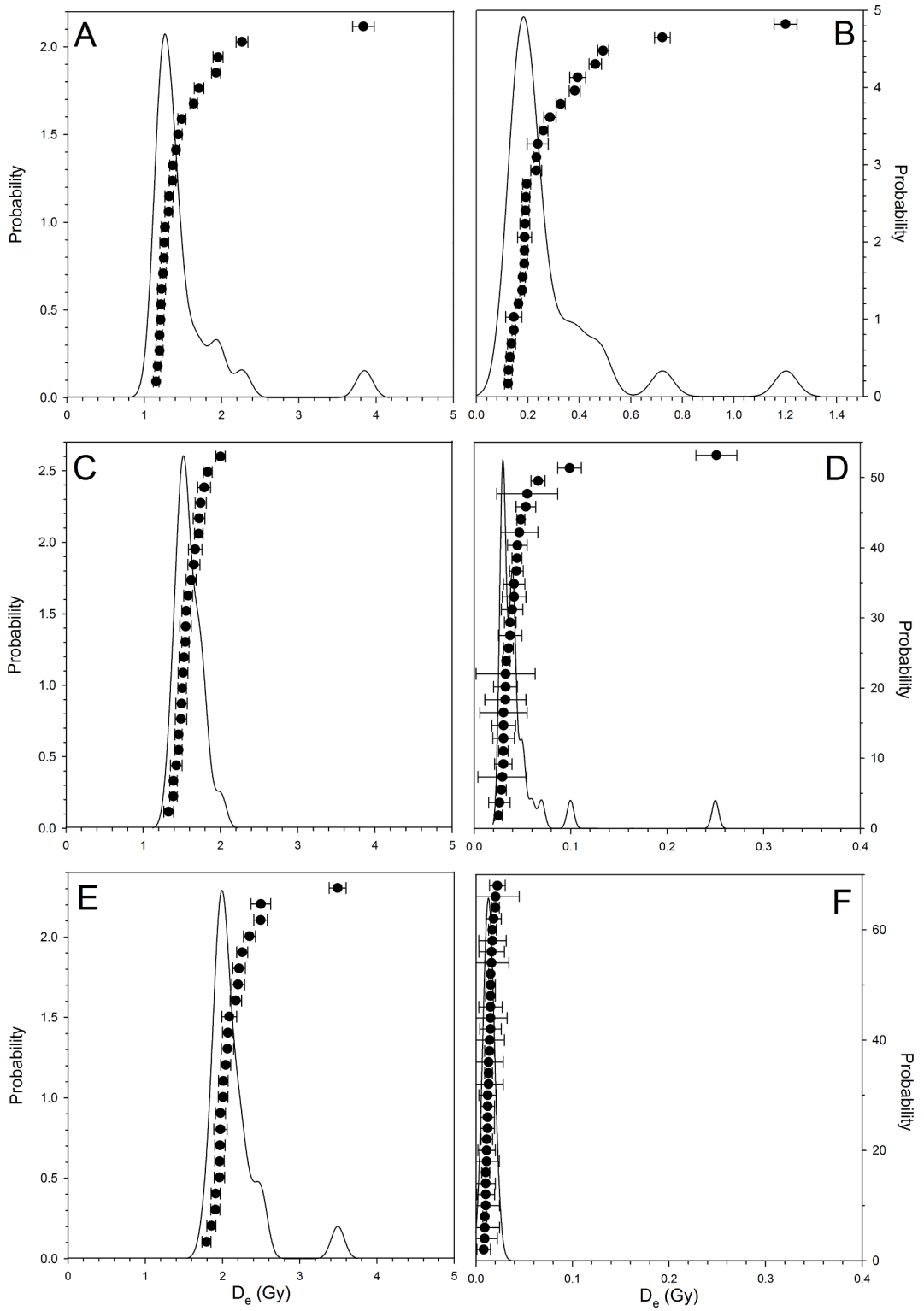

Fig. 11. Examples of D_e distributions plots reflecting the variability observed in for the samples under consideration. A: CHU-3. B: CHU-4. C: CHU-14. D: CHU-23. E: CHU-28. F: CHU-30. Most samples show a pronouinced peak of D_e values at the lower edge of the distribution, which is interpreted to reflect the average dose absorbed during burial. The higher values present above the lower edge may result from either partical resetting of the OSL signal at the time of deposition or from large beat-dose inhomogeneity effects.

This interpretation is supported by RSL records along the Thai coastline of the Western Gulf of Thailand (Choowong et al., 2004; Surakiatchai et al., 2018, 2019; Williams et al., 2016). Additionally, palaeo-beach ridges at the Chumphon estuary, around 50 km south of the Bang Berd dune field, record a sea level fall until 3.8–1.6 ka based on OSL data (Nimnate et al., 2015), which is in line with our age data for the onset of coastal dune formation (Fig. 14). Similar data from beach ridges further north along the coast at Pran Buri, Sam Roi Yot and Kui Buri (ca. 150 km from Bang Berd Bay), however, indicate that sea level was potentially still dropping 1850 years (Surakiatchai et al., 2018) and 900 years ago

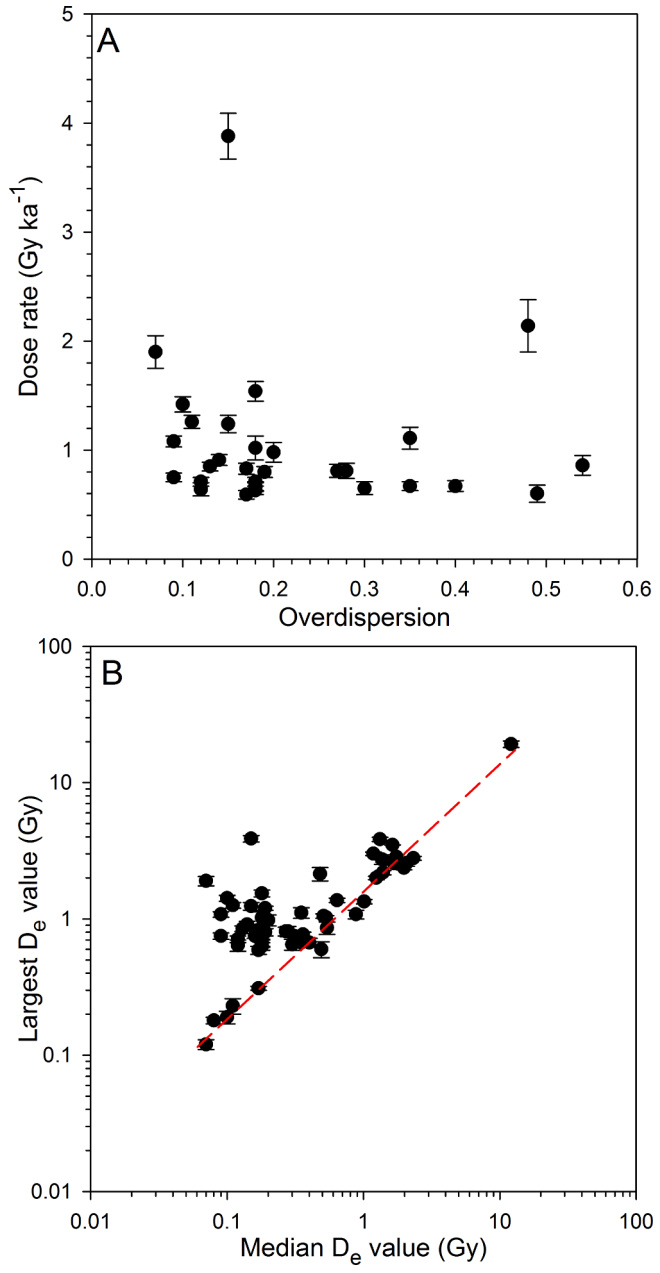

Fig. 12. Investigating the source of overdispersion. A: The comparison of dose rate and overdispersion reveals no direct relationship. B: Comparing the largest individual D_e value determined for a sample with the median D_e values of the entire distribution. The latter is representing the highest density of values. It is shown that while for part of the samples the highest D_e value is part of the main (median) distribution, several samples show outliers that are more than one order of magnitude higher.

(Surakiatchai et al., 2019), respectively.

5.2. Dune formation and climate change

While sea level changes formed the coastal geomorphological setting that allowed for the development of a dune field, the transport and deposition of the sand was likely related to monsoonal winds, as indicated by the dipping of aeolian foreset beds. The Gulf of Thailand is close to the boundary of the Asian monsoon sub-systems, Indian Summer Monsoon, East Asian Summer Monsoon and Western North Pacific Monsoon (Wang et al., 2003). Therefore, monsoon intensity and its temporal variations control environmental changes in the region. An analysis of air mass back-trajectories retrieved from NOAA's Hybrid Single Particle Langarian Integrated Trajectory Model (HYSPLIT4; Stein et al., 2015) over the last forty years (1978–2018) indicates that air moisture responsible for precipitation at the study area comes to 52% from the Indian Ocean (May-October), and the rest from the South China Sea (48%), predominantly during November and early December (Fig. 15A). Tropical storms affecting Thailand (during September-November) usually move in from the western North Pacific Ocean or the South China Sea. Nearly no precipitation occurs from mid-December to April. Wind directions reconstructed with the ERA-20C ensemble (Poli et al., 2016) for the study area (Fig. 15B) highlight the two dominant wind directions, namely SW and NE. The latter is related to the winter monsoon (November-January), while the SW winds occur during the summer monsoon (May-October). The wind directions recorded in the sedimentary structures indicate that deposition generally occurred under NE wind conditions, common during the winter monsoon. As high surface moisture hinders aeolian transport (e.g. Davidson-Arnott et al., 2008), the dune formation likely occurred during the dry months of the winter monsoon with strong winds (December-February). This highlights that the deposition of the Bang Berd dune is strongly related to monsoonal activity in the region. Note that the control of wind directions on dune formation can also be observed by the lack of coastal dunes in the north-eastern part of the Gulf of Thailand. There, NE winds cancel the onshore sand transport while SW winds are essential for building coastal dunes.

To decipher whether the changes and hiatuses observed in the sedimentary record at the study site were caused by climatic factors, palaeoclimatic data for Thailand and for the Asian monsoon region are needed to assess in greater detail the spatial and temporal variability of the Asian monsoon during the last 3000 years. The spatially closest palaeo-climate records are stalagmite oxygen isotopes from Klang cave, located around 350 km southwest of the study site. While this record indicates variable rainfall for the last 2700 years, with an overall trend towards a weaker Indian Summer Monsoon (drier conditions) (Chawchai et al., 2021; Tan et al., 2019), the stalagmites record suggested dry conditions during the Medieval Climate Anomaly (MCA: CE 950–1300). However, this is in contrast with other palaeo-climatic data from northern Thailand (Chawchai et al., 2015; Yamoah et al., 2016a,b) and Cambodia (Day et al., 2012; Penny et al., 2019) which inferred wet conditions during the MCA. Thus, Hiatus A (CE 400–1300) could also be the result of reduced sedimentation rates due to wet conditions (high surface moisture) and/or a subsequent erosional event due to extreme precipitation which erased the limited sedimentary record. Notably, the sands directly above Hiatus A were deposited under southern wind conditions, indicating that the hiatus is linked to changes in prevailing wind conditions or an extreme weather event.

Hiatus B, which is indicated by palaeosoil development, dates to ca. CE 1600–1800 and does thus coincide with the Little Ice Age (LIA; CE 1500–1850) period, for which a general trend towards dry conditions was observed in the stalagmite oxygen isotope record from Klang cave (Chawchai et al., 2021; Tan et al., 2019). However, the presence of iron-hydroxides within the palaeosoil at Bang Berd hints towards wetter conditions. It is notable that there are discrepancies between palaeorecords from the western side of Mainland SE Asia, eastern side of Mainland SE Asia and the South China Sea during the LIA, with some records indicating that wet conditions prevailed (Stevens et al., 2018; Yan et al., 2011). This is because the control of precipitation on western side of SE Asia (western Thailand and Myanmar) may have been mainly the Indian Summer Monsoon as suggested by Chawchai et al. (2020) and Liu et al. (2020), but that the Pacific Walker Circulation may have been the overriding control on precipitation for the eastern part of SE Asia (Vietnam, Cambodia, and the eastern coast of the Thai-Malay peninsula) as proposed by Yan et al. (2011) and Stevens et al. (2018). Taking this into account, Hiatus B is interpreted be the result of a wet period where aeolian deposition was limited and strong vegetation limited erosion and transport within the dune field and a paleosoil could develop.

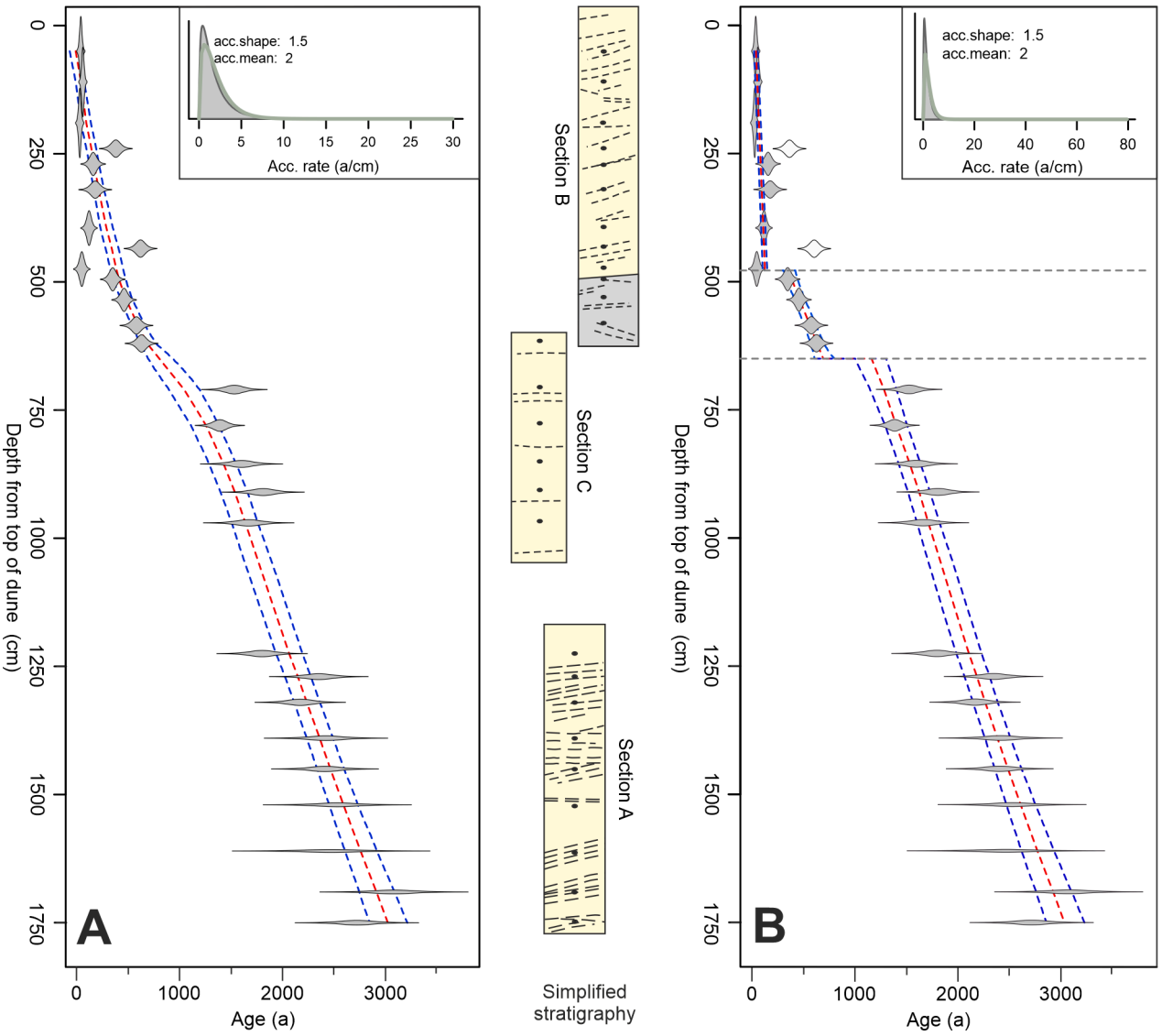

Fig. 13. Age-depth models of the studied dune based on the Bayesian statistics modelling package rbacon version 2.5.7 (Blaauw et al., 2021). OSL ages, including errors, are indicated in grey, the red dashed line is the mean and blue dashed lines are the 95% confidence intervals of the age-depth model. Accumulation rate is shown in the insets. A: Assuming constant sedimentation and taking into account all age data. B: Based on the observed palaeo-soil formation a sedimentation hiatus at 480 cm depth (17.0 m asl) is assumed. Another hiatus is assumed at 650 cm depth (15.5 m asl) due to the sudden change in sediment age. Samples CHU-20 and CHU 24 have been disregarded from this model (see text for discussion).

While deposition rates are constant between 3000 and 400 years ago, taking the hiatuses into account, sedimentation occurred faster by five times in the last ca. 200 years. Interestingly, paleoclimatic studies and rainfall monitoring data suggest that El Nino – Southern Oscillation (ENSO) events had an influence on monsoonal rainfall and strength in SE Asia on a decadal scale in the last 200 years (e.g. Abram et al., 2020; Limsakul and Singhruck, 2016; Pumijumnong et al., 2020; Räsänen et al., 2016; Tan et al., 2019). This could have led to more frequent storm events which subsequently induced higher rates of aeolian transport and deposition.

5.3. *Implications for future coastal evolution*

As sea-level changes have controlled coastal aeolian sedimentation at the study site in the past, future sea-level changes are likely to impact the sedimentary system. Sea-level is predicted to rise at least 0.5 m to 1 m within the next century (e.g., Kulp and Strauss, 2019), with extreme sea levels (high tides plus extreme storm events) in the tropics becoming much more frequent with coastal areas in SE Asia experiencing present-day 100-year events annually by CE 2050 (Vousdoukas et al., 2018). The beach at Bang Berd Bay has a flat profile and even a moderate rise in sea level will decrease the area from which sand can be supplied to the coastal dunes dramatically. The current storm line is close to the dune foot and a rise in extreme sea level would lead to the erosion of the dune and subsequently to a higher risk of flooding for the lowlying area inland of the dune field which is currently agricultural land. As a reponse to sea level rise the dune field may migrate further inland, displacing the agricultural area.

While the number of tropical storms making landfall in Thailand have decreased in the past 70 years (Lee et al., 2020), the intensity of these storms is predicted to increase in the changing climate (Cha et al., 2020). As the hiatuses observed in the sedimentary record of the studied dune can be interpreted as the result of erosional events, an increase in storm intensity may lead to significant erosion of the coastal dunes and transport sand further inland. Models indicate that the East Asian Winter Monsoon will increase in the future (Chowdary et al., 2019), which could lead to an increase in aeolian transport and sedimentation at the study site. On the other hand East Asian Summer Monsoon is expected to

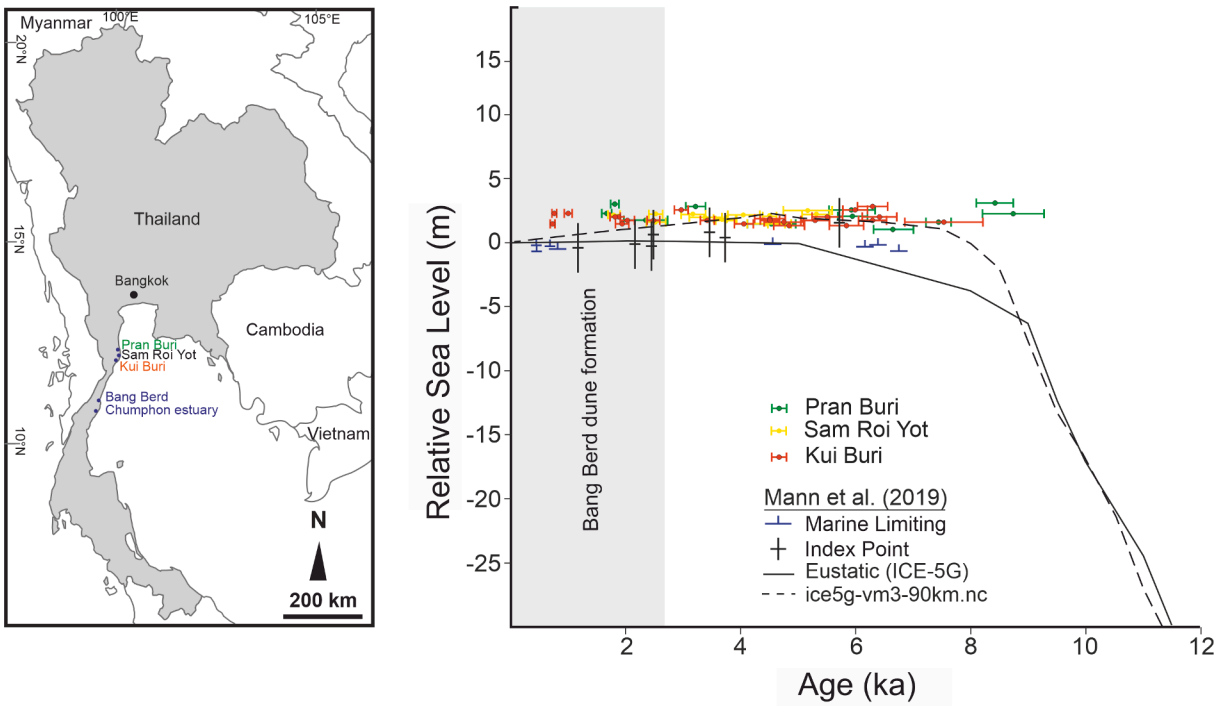

Fig. 14. Index map and relative sea-level curves including previously published OSL data from beach ridges of Pran Buri, Sam Roi Yot and Kui Buri (Surakiatchai et al., 2019) in comparison with standardized Holocene relative sea-level data of SE Asia. Error bars indicate the uncertainties of the OSL ages. The time range of dune formation at the study site is also indicated.

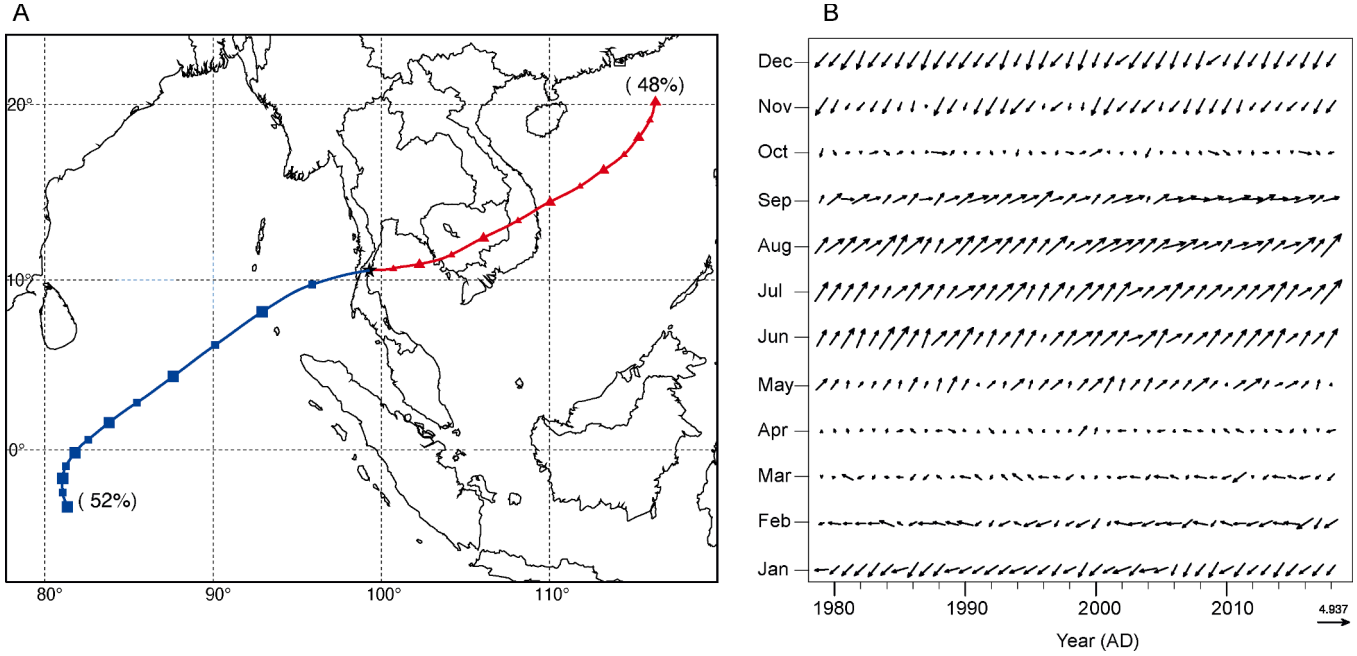

Fig. 15. A: Two primary source moisture regions to 10°56′N, 99°29′E (star). The plot is based on a cluster analysis of rain-bearing 6-day back-trajectories, simulated with NOAA's Hybrid Single Particle Langarian Integrated Trajectory (HYSPLIT4) model (Draxler and Hess, 1998; Stein et al., 2015). Blue indicates Indian Summer Monsoon source (52%) and red colour indicate East Asian Monsoon moisture source regions (48%) based on a K-means cluster analysis. B: Monthly wind direction for the study site from 1978 to 2018 derived from ERA-20C (Poli et al., 2016). (For interpretation of the references to colour in this figure legend, the reader is referred to the web version of this article.)

have an increased variability with more frequent extreme precipitation events (Tan et al., 2021), which could lead to increased erosion of the dunes. Overall, climate change is more likely to impact the dunes, which form an important coastal barrier, negatively.

6. Conclusions

High resolution OSL dating of a coastal dune within the Bang Berd Bay dune field in southern Thailand shows that deposition of the dune started at least 3000 years ago and continues until today. This study adds

important palaeoenvironmental information for the region and allows us to examine the sedimentary dynamics in the context of sea level change and varying hydroclimatic conditions. The onset of dune formation appears to be linked to sea level regression after a mid-Holocene high-stand. Sedimentary structures indicate that deposition occurred predominantly under NE wind conditions which highlights that the deposition of the coastal dune is strongly related to monsoonal activity. Sedimentation was not constant as indicated by the presence of a palaeosoil horizon and gaps in the chronology, with two hiatuses between CE 400–1300 and CE 1600–1800. Deposition of sand primarily took place in the winter months when dry conditions and NE winds related to the winter monsoon prevailed. The observed hiatuses may be linked to climatic changes recorded in paleoclimatic archives in the region. Our study highlights how sea level changes and monsoonal variability can shape coastal morphology in SE Asia. However, the late Holocene sea-level lowering along with inferred moisture and wind availability at Bang Berd dune needs to be constrained by further high-resoltuion chronologies to enable for comparisons to regional high-resolution palaeoclimatic records, and to decipher whether the changes seen in sediment were caused due to climatic factors.

CRediT authorship contribution statement

Johannes M. Miocic: Conceptualization, Investigation, Formal analysis, Visualization, Writing – original draft, Writing – review & editing. **Ritu Sah:** Investigation, Formal analysis. **Sakonvan Chawchai:** Conceptualization, Investigation, Formal analysis, Visualization, Writing – original draft, Writing – review & editing. **Peerasit Surakiatchai:** Investigation, Formal analysis. **Montri Choowong:** Supervision, Funding acquisition. **Frank Preusser:** Conceptualization, Investigation, Formal analysis, Visualization, Writing – original draft, Writing – review & editing, Supervision, Funding acquisition.

Declaration of Competing Interest

The authors declare that they have no known competing financial interests or personal relationships that could have appeared to influence the work reported in this paper.

Acknowledgements

The authors wish to express their appreciation for the financial support provided by Wissenschaftliche Gesellschaft Freiburg im Breisgau. SC and FP acknowledge Sci-Super Plus 2564, Faculty of Science, Thailand Science research and Innovation Fund Chulalongkorn University (CU_FRB65_dis (10)_098_23_28) for promoting this international research collaboration. We also thank Armelle Ballian, Stapana Kongsen and Lukped for their valuable help during field work, Alexander Fülling and Jennifer Wolff for support of the OSL dating laboratory work, and Daniela Mueller for advice regarding r-scripts. We gratefully acknowledge the comments by two reviewers on an earlier version of the manuscript.

References

Abram, N.J., Wright, N.M., Ellis, B., Dixon, B.C., Wurtzel, J.B., England, M.H., Ummenhofer, C.C., Philibosian, B., Cahyarini, S.Y., Yu, T.-L., Shen, C.-C., Cheng, H., Edwards, R.L., Heslop, D., 2020. Coupling of Indo-Pacific climate variability over the last millennium. Nature 579 (7799), 385–392. https://doi.org/10.1038/s41586-020-2084-4.

Adams, J.A.S., Weaver, C.E., 1958. Thorium-to-uranium ratios as indicators of sedimentary processes: example of concept of geochemical facies1. AAPG Bull. 42, 387–430. https://doi.org/10.1306/0BDA5A89-16BD-11D7-8645000102C1865D.

Bateman, M.D., Rushby, G., Stein, S., Ashurst, R.A., Stevenson, D., Jones, J.M., Gehrels, W.R., 2018. Can sand dunes be used to study historic storm events? Earth Surf. Process. Landf. 43 (4), 779–790. https://doi.org/10.1002/esp.v43.410.1002/esp.4255.

Bauer, B.O., Davidson-Arnott, R.G.D., 2003. A general framework for modeling sediment supply to coastal dunes including wind angle, beach geometry, and fetch effects. Geomorphology 49 (1-2), 89–108. https://doi.org/10.1016/S0169-555X(02)00165-4.

Bird, M.I., Austin, W.E.N., Wurster, C.M., Fifield, L.K., Mojtahid, M., Sargeant, C., 2010. Punctuated eustatic sea-level rise in the early mid-Holocene. Geology 38, 803–806. https://doi.org/10.1130/G31066.1.

Bird, M.I., Fifield, L.K., Teh, T.S., Chang, C.H., Shirlaw, N., Lambeck, K., 2007. An inflection in the rate of early mid-Holocene eustatic sea-level rise: a new sea-level curve from Singapore. Estuar. Coast. Shelf Sci. 71 (3-4), 523–536. https://doi.org/10.1016/j.ecss.2006.07.004.

Blaauw, M., Christen, J.A., 2011. Flexible paleoclimate age-depth models using an autoregressive gamma process. Bayesian Anal. 6, 457–474. https://doi.org/10.1214/11-BA618.

Blaauw, M., Christen, J.A., Lopez, M.A.A., Vazquez, J.E., V, O.M.G., Belding, T., Theiler, J., Gough, B., Karney, C., 2021. rbacon: Age-Depth Modelling using Bayesian Statistics.

Blott, S.J., Pye, K., 2001. GRADISTAT: a grain size distribution and statistics package for the analysis of unconsolidated sediments. Earth Surf. Process. Landf. 26 (11), 1237–1248. https://doi.org/10.1002/esp.v26:1110.1002/esp.261.

Brill, D., Jankaew, K., Brückner, H., 2015. Holocene evolution of Phra Thong's beach-ridge plain (Thailand) — Chronology, processes and driving factors. Geomorphology 245, 117–134. https://doi.org/10.1016/j.geomorph.2015.05.035.

Burow, C., 2020. calc_MinDose: Apply the (un-)logged minimum age model (MAM) after Galbraith et al. (1999) to a given De distribution. Function version 0.4.4. In: Kreutzer, S., Burow, C., Dietze, M., Fuchs, M.C., Schmidt, C., Fischer, M., Friedrich, J., Riedesel, S., Autzen, M., Mittelstrass, D., 2020. Luminescence: Comprehensive Luminescence Dating Data Analysis. R package version 0.9.10. https://cran.r-project.org/package=Luminescence.

Burow, C., 2020. calc_CentralDose: Apply the central age model (CAM) after Galbraith et al. (1999) to a given De distribution. Function version 1.4.0. In: Kreutzer, S., Burow, C., Dietze, M., Fuchs, M.C., Schmidt, C., Fischer, M., Friedrich, J., Riedesel, S., Autzen, M., Mittelstrass, D., 2020. Luminescence: Comprehensive Luminescence Dating Data Analysis. R package version 0.9.10. https://cran.r-project.org/package=Luminescence.

Buynevich, I.V., 2012. Morphologically induced density lag formation on bedforms and biogenic structures in aeolian sands. Aeolian Res. Aeolian Process. Biophys. Drivers Biogeochem. Impl. 7, 11–15. https://doi.org/10.1016/j.aeolia.2011.12.005.

Cha, E.J., Knutson, T.R., Lee, T.-C., Ying, M., Nakaegawa, T., 2020. Third assessment on impacts of climate change on tropical cyclones in the Typhoon Committee Region – Part II: Future projections. Trop. Cyclone Res. Rev. 9 (2), 75–86. https://doi.org/10.1016/j.tcrr.2020.04.005.

Chawchai, S., Chabangborn, A., Fritz, S., Väliranta, M., Mörth, C.-M., Blaauw, M., Reimer, P.J., Krusic, P.J., Löwemark, L., Wohlfarth, B., 2015. Hydroclimatic shifts in northeast Thailand during the last two millennia – the record of Lake Pa Kho. Quat. Sci. Rev. 111, 62–71. https://doi.org/10.1016/j.quascirev.2015.01.007.

Chawchai, S., Tan, L., Löwemark, L., Wang, H.-C., Yu, T.-L., Chung, Y.-C., Mii, H.-S., Liu, G., Blaauw, M., Gong, S.-Y., Wohlfarth, B., Shen, C.-C., 2021. Hydroclimate variability of central Indo-Pacific region during the Holocene. Quat. Sci. Rev. 253, 106779. https://doi.org/10.1016/j.quascirev.2020.106779.

Choowong, M., 2011. Quaternary. https://doi.org/10.1144/GOTH.12.

Choowong, M., Ugai, H., Charoentitirat, T., Charusiri, P., Daorerk, V., Songmuang, R., Ladachart, R., 2004. Holocene biostratigraphical records in coastal deposits from sam Roi Yod National Park, Prachuap Khiri Khan, Western Thailand. Trop. Nat. Hist. 4, 1–18.

Chowdary, J.S., Hu, K., Srinivas, G., Kosaka, Y.u., Wang, L., Rao, K.K., 2019. The eurasian Jet streams as conduits for east asian monsoon variability. Curr. Clim. Change Rep. 5 (3), 233–244. https://doi.org/10.1007/s40641-019-00134-x.

Clemmensen, L.B., Murray, A., 2006. The termination of the last major phase of aeolian sand movement, coastal dunefields, Denmark. Earth Surf. Process. Landf. 31 (7), 795–808. https://doi.org/10.1002/esp.1283.

Clemmensen, L.B., Pye, K., Murray, A., Heinemeier, J., 2001. Sedimentology, stratigraphy and landscape evolution of a Holocene coastal dune system, Lodbjerg, NW Jutland, Denmark. Sedimentology 48, 3–27. https://doi.org/10.1111/j.1365-3091.2001.00345.x.

Davidson-Arnott, R.G.D., Yang, Y., Ollerhead, J., Hesp, P.A., Walker, I.J., 2008. The effects of surface moisture on aeolian sediment transport threshold and mass flux on a beach. Earth Surf. Process. Landf. 33 (1), 55–74. https://doi.org/10.1002/esp.1527.

Day, M.B., Hodell, D.A., Brenner, M., Chapman, H.J., Curtis, J.H., Kenney, W.F., Kolata, A.L., Peterson, L.C., 2012. Paleoenvironmental history of the West Baray, Angkor (Cambodia). Proc. Natl. Acad. Sci. 109 (4), 1046–1051. https://doi.org/10.1073/pnas.1111282109.

Degering, D., Degering, A., 2020. Change is the only constant - time-dependent dose rates in luminescence dating. Quat. Geochronol. 58, 101074. https://doi.org/10.1016/j.quageo.2020.101074.

Devi, K., Raicy, M.C., Trivedi, D., Srinivasan, P., Murthy, S.G.N., Goble, R.J., Nair, R.R., 2013. Assessment of coastal dune characteristics using georadar imaging and sedimentological analysis: Odisha and Visakhapatnam, India. J. Coast. Conserv. 17 (4), 729–742. https://doi.org/10.1007/s11852-013-0272-1.

Draxler, R.R., Hess, G., 1998. An overview of the HYSPLIT_4 modelling system for trajectories. Aust. Meteorol. Mag. 47, 295–308.

Galbraith, R.F., Roberts, R.G., 2012. Statistical aspects of equivalent dose and error calculation and display in OSL dating: an overview and some recommendations. Quat. Geochronol. 11, 1–27. https://doi.org/10.1016/j.quageo.2012.04.020.

Heiri, O., Lotter, A.F., Lemcke, G., 2001. Loss on ignition as a method for estimating organic and carbonate content in sediments: reproducibility and comparability of results. J. Paleolimnol. 25, 101–110. https://doi.org/10.1023/A:1008119611481.

Hesp, P.A., 2004. Coastal dunes in the tropics and temperate regions: location, formation, morphology and vegetation processes. In: Martínez, M.L., Psuty, N.P. (Eds.), Coastal Dunes: Ecology and Conservation, Ecological Studies. Springer, Berlin, Heidelberg, pp. 29–49. https://doi.org/10.1007/978-3-540-74002-5_3.

Hesp, P.A., Hung, C.C., Hilton, M., Ming, C.L., Turner, I.M., 1998. A first tentative holocene sea-level curve for singapore. J. Coast. Res. 14, 308–314.

Horton, B.P., Gibbard, P.L., Mine, G.M., Morley, R.J., Purintavaragul, C., Stargardt, J.M., 2005. Holocene sea levels and palaeoenvironments, Malay-Thai Peninsula, southeast Asia. Holocene 15 (8), 1199–1213. https://doi.org/10.1191/0959683605hl891rp.

Hunter, R.E., Richmond, B.M., 1988. Daily cycles in coastal dunes. Sediment. Geol. Eolian Sediments 55 (1-2), 43–67. https://doi.org/10.1016/0037-0738(88)90089-9.

Kulp, S.A., Strauss, B.H., 2019. New elevation data triple estimates of global vulnerability to sea-level rise and coastal flooding. Nat. Commun. 10, 4844. https://doi.org/10.1038/s41467-019-12808-z.

Laongpol, C., Suzuki, K., Katzensteiner, K., Sridith, K., 2009. Plant community structure of the coastal vegetation of peninsular Thailand. Thai For. Bull. Bot. 106–133.

Lee, T.-C., Knutson, T.R., Nakaegawa, T., Ying, M., Cha, E.J., 2020. Third assessment on impacts of climate change on tropical cyclones in the Typhoon Committee Region – Part I: Observed changes, detection and attribution. Trop. Cyclone Res. Rev. 9 (1), 1–22. https://doi.org/10.1016/j.tcrr.2020.03.001.

Lees, B., 2006. Timing and formation of coastal dunes in northern and eastern Australia. J. Coast. Res. 22, 78–89. https://doi.org/10.2112/05A-0007.1.

Lertnok, W., Choowong, M., Thitimakorn, T., 2009. Geomorphology and ground penetrating radar profiles of holocene coastal dune, western coastal plain of the gulf of Thailand. Bull. Earth Sci. Thail. 3, 17–27.

Limsakul, A., Singhruck, P., 2016. Long-term trends and variability of total and extreme precipitation in Thailand. Atmos. Res. 169, 301–317. https://doi.org/10.1016/j.atmosres.2015.10.015.

Liu, G., Li, X., Chiang, H.-W., Cheng, H., Yuan, S., Chawchai, S., He, S., Lu, Y., Aung, L.T., Maung, P.M., Tun, W.N., Oo, K.M., Wang, X., 2020. On the glacial-interglacial variability of the Asian monsoon in speleothem δ18O records. Sci. Adv. 6, eaay8189. https://doi.org/10.1126/sciadv.aay8189.

Mann, T., Bender, M., Lorscheid, T., Stocchi, P., Vacchi, M., Switzer, A.D., Rovere, A., 2019. Holocene sea levels in Southeast Asia, Maldives, India and Sri Lanka: The SEAMIS database. Quat. Sci. Rev. 219, 112–125. https://doi.org/10.1016/j.quascirev.2019.07.007.

Marod, D., Sungkaew, S., Mizunaga, H., Thinkampheang, S., Thongsawi, J., 2020. Woody plant community and distribution in a tropical coastal sand dune in southern Thailand. J. Coast. Conserv. 24, 44. https://doi.org/10.1007/s11852-020-00761-9.

Mayya, Y.S., Morthekai, P., Murari, M.K., Singhvi, A.K., 2006. Towards quantifying beta microdosimetric effects in single-grain quartz dose distribution. Radiat. Meas. 41 (7-8), 1032–1039. https://doi.org/10.1016/j.radmeas.2006.08.004.

Meltzner, A.J., Switzer, A.D., Horton, B.P., Ashe, E., Qiu, Q., Hill, D.F., Bradley, S.L., Kopp, R.E., Hill, E.M., Majewski, J.M., Natawidjaja, D.H., Suwargadi, B.W., 2017. Half-metre sea-level fluctuations on centennial timescales from mid-Holocene corals of Southeast Asia. Nat. Commun. 8, 1–16. https://doi.org/10.1038/ncomms14387.

Miot da Silva, G., Hesp, P., 2010. Coastline orientation, aeolian sediment transport and foredune and dunefield dynamics of Moçambique Beach, Southern Brazil. Geomorphology 120 (3-4), 258–278. https://doi.org/10.1016/j.geomorph.2010.03.039.

Morton, R.A., Gelfenbaum, G., Jaffe, B.E., 2007. Physical criteria for distinguishing sandy tsunami and storm deposits using modern examples. Sediment. Geol Sedimen. Features Tsunami Depos. 200 (3-4), 184–207. https://doi.org/10.1016/j.sedgeo.2007.01.003.

Murray, A.S., Wintle, A.G., 2000. Luminescence dating of quartz using an improved single-aliquot regenerative-dose protocol. Radiat. Meas. 32 (1), 57–73. https://doi.org/10.1016/S1350-4487(99)00253-X.

NASA/METI/AIST/Japan Spacesystems And U.S./Japan ASTER Science Team, 2019. ASTER Global Digital Elevation Model V003. https://doi.org/10.5067/ASTER/ASTGTM.003.

Neal, W.J., Pilkey, O.H., Cooper, J.A.G., Longo, N.J., 2018. Why coastal regulations fail. Ocean Coast. Manag. SI MSforCEP 156, 21–34. https://doi.org/10.1016/j.ocecoaman.2017.05.003.

Neudorf, C.M., Lian, O.B., Walker, I.J., Shugar, D.H., Eamer, J.B.R., Griffin, L.C.M., 2015. Toward a luminescence chronology for coastal dune and beach deposits on Calvert Island, British Columbia central coast, Canada. Quat. Geochronol., LED14 Proceedings 30, 275–281. https://doi.org/10.1016/j.quageo.2014.12.004.

Nimnate, P., Chutakositkanon, V., Choowong, M., Pailoplee, S., Phantuwongraj, S., 2015. Evidence of Holocene sea level regression from Chumphon coast of the Gulf of Thailand. ScienceAsia 41 (1), 55. https://doi.org/10.2306/scienceasia1513-1874.2015.41.055.

Noppradit, P., Schmidt, C., Dürrast, H., Zöller, L., 2019. Late Quaternary evolution of Songhkla coast, Southern Thailand, revealed by OSL dating. Chiang Mai J. Sci. 46, 152–164.

Olley, J.M., De Deckker, P., Roberts, R.G., Fifield, L.K., Yoshida, H., Hancock, G., 2004. Optical dating of deep-sea sediments using single grains of quartz: a comparison with radiocarbon. Sediment. Geol. 169 (3-4), 175–189. https://doi.org/10.1016/j.sedgeo.2004.05.005.

Oppenheimer, D.H., Glavovic, B.C., Hinkel, J., 2019. Chapter 4: Sea Level Rise and Implications for Low-Lying Islands, Coasts and Communities — Special Report on the Ocean and Cryosphere in a Changing Climate.

Parham, Peter.R., Saito, Yoshiki, Sapon, Noraisyah, Suriadi, Rokiah, Mohtar, Noor. Azariyah., 2014. Evidence for ca. 7-ka maximum Holocene transgression on the Peninsular Malaysia east coast. J. Quat. Sci. 29 (5), 414–422. https://doi.org/10.1002/jqs.2714.

Penny, D., Hall, T., Evans, D., Polkinghorne, M., 2019. Geoarchaeological evidence from Angkor, Cambodia, reveals a gradual decline rather than a catastrophic 15th-century collapse. Proc. Natl. Acad. Sci. 116 (11), 4871–4876. https://doi.org/10.1073/pnas.1821460116.

Phantuwongraj, S., Choowong, M., Nanayama, F., Hisada, K.-I., Charusiri, P., Chutakositkanon, V., Pailoplee, S., Chabangbon, A., 2013. Coastal geomorphic conditions and styles of storm surge washover deposits from Southern Thailand. Geomorphology 192, 43–58. https://doi.org/10.1016/j.geomorph.2013.03.016.

Poli, P., Hersbach, H., Dee, D.P., Berrisford, P., Simmons, A.J., Vitart, F., Laloyaux, P., Tan, D.G.H., Peubey, C., Thépaut, J.-N., Trémolet, Y., Hólm, E.V., Bonavita, M., Isaksen, L., Fisher, M., 2016. ERA-20C: an atmospheric reanalysis of the twentieth century. J. Clim. 29, 4083–4097. https://doi.org/10.1175/JCLI-D-15-0556.1.

Prachantasen, N., Choowong, M., Pailoplee, S., Phantuwongraj, S., 2008a. Sedimentary characteristics of sand dune from Bang Berd, Chumphon Province, Southern Thailand. Bull. Earth Sci. Thail. BEST 1, 28–34.

Prachantasen, N., Choowong, M., Pailoplee, S., Phantuwongraj, S., 2008b. Sedimentary characteristics of sand dune from Bang Berd, Chumphon Province, Southern Thailand. Bull. Earth Sci. Thail. 1, 28–34.

Preusser, F., Kasper, H.U., 2001. Comparison of dose rate determination using high-resolution gamma spectrometry and inductively coupled plasma-mass spectrometry. Anc. TL 19, 19–23. https://doi.org/10.7892/boris.86818.

Pumijumnong, N., Bräuning, A., Sano, M., Nakatsuka, T., Muangsong, C., Buajan, S., 2020. A 338-year tree-ring oxygen isotope record from Thai teak captures the variations in the Asian summer monsoon system. Sci. Rep. 10, 8966. https://doi.org/10.1038/s41598-020-66001-0.

Pye, K., 1983. Coastal dunes. Prog. Phys. Geogr. Earth Environ. 7 (4), 531–557. https://doi.org/10.1177/030913338300700403.

Pye, K., Tsoar, H. (Eds.), 2009. Aeolian Sand and Sand Dunes. Springer Berlin Heidelberg, Berlin, Heidelberg.

Rangel-Buitrago, N., Williams, A.T., Anfuso, G., 2018. Hard protection structures as a principal coastal erosion management strategy along the Caribbean coast of Colombia. A chronicle of pitfalls. Ocean Coast. Manag, SI: MSforCEP 156, 58–75. https://doi.org/10.1016/j.ocecoaman.2017.04.006.

Räsänen, T.A., Lindgren, V., Guillaume, J.H.A., Buckley, B.M., Kummu, M., 2016. On the spatial and temporal variability of ENSO precipitation and drought teleconnection in mainland Southeast Asia. Clim. Past 12 (9), 1889–1905. https://doi.org/10.5194/cp-12-1889-2016.

Sancho, F., Oliveira, F.S.B.F., Freire, P., 2012. Coastal dunes vulnerability indexes: a new proposal. Coast. Eng. Proc. 1 (33), 68. https://doi.org/10.9753/icce:v33.management.68.

Scheffers, A., Brill, D., Kelletat, D., Brückner, H., Scheffers, S., Fox, K., 2012. Holocene sea levels along the Andaman Sea coast of Thailand. Holocene 22 (10), 1169–1180. https://doi.org/10.1177/0959683612441803.

Sherman, D.J., Lyons, W., 1994. Beach-state controls on aeolian sand delivery to coastal dunes. Phys. Geogr. 15 (4), 381–395. https://doi.org/10.1080/02723646.1994.10642524.

Sommerville, A.A., Hansom, J.D., Housley, R.A., Sanderson, D.C.W., 2007. Optically stimulated luminescence (OSL) dating of coastal aeolian sand accumulation in Sanday, Orkney Islands, Scotland. Holocene 17 (5), 627–637. https://doi.org/10.1177/0959683607078987.

Speer, J.A., 1980. CHAPTER 3. ZIRCON, Orthosilicates. De Gruyter.

Stein, A.F., Draxler, R.R., Rolph, G.D., Stunder, B.J.B., Cohen, M.D., Ngan, F., 2015. NOAA's HYSPLIT Atmospheric Transport and Dispersion Modeling System. Bull. Am. Meteorol. Soc. 96, 2059–2077. https://doi.org/10.1175/BAMS-D-14-00110.1.

Stevens, L.R., Buckley, B.M., Kim, S., Hill, P., Doiron, K., 2018. Increased effective moisture in northern Vietnam during the Little Ice Age. Palaeogeogr. Palaeoclimatol. Palaeoecol. 511, 449–461. https://doi.org/10.1016/j.palaeo.2018.09.011.

Surakiatchai, P., Choowong, M., Charusiri, P., Charoentitirat, T., Chawchai, S., Pailoplee, S., Chabangborn, A., Phantuwongraj, S., Chutakositkanon, V., Kongsen, S., Nimnate, P., Bissen, R., 2018. Paleogeographic reconstruction and history of the sea level change at sam roi yot national park, gulf of Thailand. Trop. Nat. Hist. 18, 112–134.

Surakiatchai, P., Songsangworn, E., Pailoplee, S., Choowong, M., Phantuwongraj, S., Chabangborn, A., Charusiri, P., 2019. Optically stimulated luminescence dating reveals rate of beach ridge and sand spit depositions from the upper Gulf of Thailand. Songklanakarin J. Sci. Technol. 41.

Tamura, T., Bateman, M.D., Kodama, Y., Saitoh, Y.u., Watanabe, K., Yamaguchi, N., Matsumoto, D., 2011. Building of shore-oblique transverse dune ridges revealed by ground-penetrating radar and optical dating over the last 500years on Tottori coast, Japan Sea. Geomorphology 132 (3-4), 153–166. https://doi.org/10.1016/j.geomorph.2011.05.005.

Tamura, T., Ta, T.K.O., Saito, Y., Bateman, M.D., Murray-Wallace, C.V., Nguyen, T.M.L., Sato, T., Nguyen, V.L., 2020. Seasonal control on coastal dune morphostratigraphy under a monsoon climate, Mui Ne dunefield, SE Vietnam. Geomorphology 370, 107371. https://doi.org/10.1016/j.geomorph.2020.107371.

Tan, L., Li, Y., Han, W., 2021. A paleoclimate prognosis of the future asian summer monsoon variability. Atmosphere 12, 1391. https://doi.org/10.3390/atmos12111391.

Tan, L., Shen, C.-C., Löwemark, L., Chawchai, S., Edwards, R.L., Cai, Y., Breitenbach, S.F. M., Cheng, H., Chou, Y.-C., Duerrast, H., Partin, J.W., Cai, W., Chabangborn, A., Gao, Y., Kwiecien, O., Wu, C.-C., Shi, Z., Hsu, H.-H., Wohlfarth, B., 2019. Rainfall variations in central Indo-Pacific over the past 2,700 y. Proc. Natl. Acad. Sci. 116 (35), 17201–17206. https://doi.org/10.1073/pnas.1903167116.

Tindahl Madsen, A., Murray, A.S., Joest Andersen, T., 2007. Optical dating of dune ridges on rømø, a barrier island in the wadden sea. Denmark. J. Coast. Res. 23, 1259–1269. https://doi.org/10.2112/05-0471.1.

Tribolo, C., Mercier, N., Rasse, M., Soriano, S., Huysecom, E., 2010. Kobo 1 and L'Abri aux Vaches (Mali, West Africa): Two case studies for the optical dating of bioturbated sediments. Quat. Geochronol. 5 (2-3), 317–323. https://doi.org/10.1016/j.quageo.2009.03.002.

Vousdoukas, M.I., Mentaschi, L., Voukouvalas, E., Verlaan, M., Jevrejeva, S., Jackson, L. P., Feyen, L., 2018. Global probabilistic projections of extreme sea levels show intensification of coastal flood hazard. Nat. Commun. 9, 2360. https://doi.org/10.1038/s41467-018-04692-w.

Wang, B., Clemens, S.C., Liu, P., 2003. Contrasting the Indian and East Asian monsoons: implications on geologic timescales. Mar. Geol., Asian Monsoons and Global Linkages on Milankovitch and Sub-Milankovitch Time Scales 201, 5–21. https://doi.org/10.1016/S0025-3227(03)00196-8.

Williams, H., Choowong, M., Phantuwongraj, S., Surakietchai, P., Thongkhao, T., Kongsen, S., Simon, E., 2016. Geologic records of Holocene typhoon strikes on the Gulf of Thailand coast. Mar. Geol. 372, 66–78. https://doi.org/10.1016/j.margeo.2015.12.014.

Wilson, P., Orford, J.D., Knight, J., Braley, S.M., Wintle, A.G., 2001. Late-Holocene (post-4000 years BP) coastal dune development in Northumberland, northeast England. Holocene 11 (2), 215–229. https://doi.org/10.1191/095968301667179797.

Yamoah, K., Chabangborn, A., Chawchai, S., Schenk, F., Wohlfarth, B., Smittenberg, R. H., 2016a. A 2000-year leaf wax-based hydrogen isotope record from Southeast Asia suggests low frequency ENSO-like teleconnections on a centennial timescale. Quat. Sci. Rev. 148, 44–53. https://doi.org/10.1016/j.quascirev.2016.07.002.

Yamoah, K., Chabangborn, A., Chawchai, S., Väliranta, M., Wohlfarth, B., Smittenberg, R.H., 2016b. Large variability in n-alkane δ13C values in Lake Pa Kho (Thailand) driven by wetland wetness and aquatic productivity. Org. Geochem. 97, 53–60. https://doi.org/10.1016/j.orggeochem.2016.04.008.

Yan, H., Sun, L., Oppo, D.W., Wang, Y., Liu, Z., Xie, Z., Liu, X., Cheng, W., 2011. South China Sea hydrological changes and Pacific Walker Circulation variations over the last millennium. Nat. Commun. 2, 293. https://doi.org/10.1038/ncomms1297.

Yu, K.B., Brook, G.A., Rhew, H., Shin, Y.H., Kim, S.H., Brook, F.Z., 2009. Episodic coastal dune development in the Taean Peninsula and Anmyeon Island, Korea, during the mid to late Holocene. J. Quat. Sci. 24, 982–990. https://doi.org/10.1002/jqs.1277.